Technical and environmental potentialities of recycled steel fiber reinforced concrete for structural applications

Cristina Frazão [a], *http://www.isise.net, Joaquim Barros [a], J. Alexandre Bogas [b], Verónica García-Cortés [c], Tiago Valente [d]

[a] ISISE, Dept. of Civil Engineering, University of Minho, Campus de Azurém, Guimarães, Portugal
[b] CERIS, Dept. of Civil Engineering, Architecture and Georesources, Instituto Superior Técnico, University of Lisbon, Portugal
[c] TECNALIA, Basque Research and Technology Alliance (BRTA), Parque Tecnológico de Bizkaia, Astondo Bidea, Edificio 700, Derio, Spain
[d] CiviTest – Pesquisa de Novos Materiais para a Eng.° Civil, Lda., Parque Industrial de Jesufrei, Vila Nova de Famalicão, Portugal

ARTICLE INFO

ABSTRACT

The use of recycled materials and industrial by-products as sustainable constituents of cement-based materials could be an environmentally and technically promising solution for application to structural elements. In the present work, the technical and environmental impact of using recycled steel fibers as an alternative to industrial steel fibers for concrete reinforcement was assessed at material level. Numerical simulations were performed to derive the post-cracking constitutive laws of the developed Recycled Steel Fiber Reinforced Concrete (RSFRC) and Industrial Steel Fiber Reinforced Concrete (ISFRC) by inverse analysis of experimental results obtained from three-point notched beam bending tests (3PNBBT), round panel tests supported in three points (RPT-3ps) and double edge wedge splitting tests (DEWST). These simulations were able of fitting with high accuracy the experimental results and consequently to derive the tensile stress-crack width relationships of RSFRC and ISFRC that was used to numerically simulate the bending response of a T-cross section steel RSFRC beam failing in shear.

The environmental impact of the incorporation of RSF in concrete in comparison with ISFRC was evaluated using Life Cycle Assessment methodology. The reduction of the environmental impact of the production of RSFRC compared to ISFRC with the same concrete strength class is demonstrated.

Nomenclature

ADP	Abiotic depletion potential
AP	Acidification Potential
BSC	Blind simulation competition
CEM	Portland cement type CEM I 42.5R
Cf	Content of fibers per concrete m^3

CG	Crushed granite
CED	Cumulative Energy Demand
CML	Centrum voor Milieuwetenschappen in Leiden
CMOD	Crack mouth opening displacement
CTOD	Crack tip opening displacement
CS	Coarse river sand
DEWST	Double edge wedge splitting test
ELCD	European Life Cycle Database
ELT	End-of-life tires
EP	Eutrophication potential
EPD	Environmental product declaration
FA	Fly ash
FE	Finite element
FEM	Finite element method
FRC	Fiber reinforced concrete
FS	Fine river sand
GFM	Global fitting module
GWP	Global warming potential
HCFCs	Halocarbons
IA	Inverse analysis
IP	Integration point(s)
ISF	Industrial steel Fibers
ISFRC	Industrial Steel Fiber Reinforced Concrete
ISFRC_REF	Reference industrial Steel Fiber Reinforced Concrete
LCA	Life Cycle Assessment
LCI	Life Cycle Inventory
NLSQ	Nonlinear least square fitting
ODP	Ozone depletion potential
PE-Re	Renewable primary energy consumption
PE-NRe	Non-renewable primary energy consumption
POCP	Photochemical ozone creation potential
PUM	Parameter updating module
R/FRC	Reinforced fiber reinforced concrete
RPT-3ps	Round panel tests supported on three points
RSF	Recycled Steel Fibers
RSFRC	Recycled Steel Fiber Reinforced Concrete
SFRC	Steel Fiber Reinforced Concrete
SFRSCC	Steel fiber reinforced self-compacting concrete
SP	Superplasticizer
W	Water
3PNBBT	Three-point notched beam bending test

1. Introduction

The climate change caused by the increased concentrations of greenhouse gas emissions and atmospheric pollution is considered one of the major challenges faced by humanity in the current century, with serious and global consequences for the environment, human health and economy [1]. The construction sector is one of the main contributors to the global warming, accounting for 36% of the total final energy use, and 39% of energy-related CO_2 emissions in 2018 [2]. In the recent years, various approaches have been promoted to reduce these CO_2 emissions and mitigate their negative environmental footprint, namely the development of sustainable materials and the minimization and reuse of waste [3–5]. In particular, the use of recycled materials and industrial by-products as sustainable constituents for cement-based materials has become an environmentally and technically goal, as it avoids landfill disposal, reduces the depletion of raw materials (due to partial to total replacement with recycled materials) and leads to the reduction of detrimental changes to the environment, by minimizing CO_2 emissions [3–6].

In the recent years, several research studies have explored the potential of end-of-life tires (ELT) by-products in the construction industry, such as the retrieval of Recycled Steel Fibers (RSF) and their use in the reinforcement of cement-based materials [5–13]. It is estimated that a total of one billion ELT is generated every year [14] and this amount is expected to increase over the next years, according to the projected global transport growth [15]. The reuse and rational disposal of ELT is a high priority goal of the tire business, since the increasing amount of this type of waste is a serious environmental and public health threat [16]. The reuse of waste tires has become the most sustainable strategy to enable the investment in ELT recycling. Approximately 15–25% by weight of a tire

is composed of metal [17]. The RSF are currently derived from the tire recycling industry, using mechanical and thermal degradation processes, such as tire shredding, cryogenic reduction and pyrolysis [6]. The use of RSF may reduce the emission of CO_2 since recycling saves impressive amounts of energy, contributing to the reduction of the ecological footprint and promoting environmental sustainability [12,13].

The reinforcement of cement-based materials with discrete steel fibers is now a current practice for several applications, such as industrial floors, tunnel linings, prefabricated elements and hydraulic structures. Steel Fiber Reinforced Concrete (SFRC) is increasingly adopted in prefabricated and in-situ concrete structures, allowing the partial or total replacement of conventional reinforcement. This reduces the construction time and labor costs related to the placement of conventional rebars. SFRC also contributes to reduce cracking due to shrinkage and to enhance the durability of concrete structures. The incorporation of Industrial Steel Fibers (ISF) in reinforced concrete to improve the mechanical and durability performance of concrete structures has been investigated over the past three decades [18–20]. The crack opening restraint provided by the reinforcement mechanism of ISF bridging the cracks [19] leads to a significant increase of the post-cracking load bearing capacity and energy absorption performance. The stress redistribution provided by fiber reinforcement allows the ultimate load to be higher than the cracking load, notably significant for structures with high degree of support redundancy [21].

According to the available bibliography, RSF derived from the tire recycling industry can be an effective reinforcement for structural and non-structural concrete, with a beneficial economic and environmental impact [5–13]. The heterogeneity of RSF in terms of geometry and surface conditions, provides a plurality of strengthening mechanisms that can be optimized for constituting an efficient reinforcement system in Recycled Steel Fiber Reinforced Concrete (RSFRC). It has been shown that RSF can significantly reduce the brittle behavior of concrete by improving its post-cracking resistance and deformation capacity [6].

Recent research demonstrates that RSF can be a viable alternative to commercially available ISF for use in SFRC, without a significant decay in the relevant mechanical properties, provided that the RSF present adequate geometric characteristics, which depend on the source (waste tires) and the recycling process [8,9]. The results of experimental and numerical investigations aiming to characterize the tensile and bond behavior of RSF embedded in cementitious matrices, as well as the compressive strength and flexural behavior of notched RSFRC beams showed that RSF may be suitable for the reinforcement of cementitious composites with enhanced ductility and toughness properties [10–12]. In addition, the replacement of ISF by RSF in fiber concrete responds to the concept of Circular Economy, as may impact on the reduction of energy consumption and greenhouse gas emissions [12,13]. However, further research is needed to explore the possibility of using RSFRC applied in structural elements, as an eco-friendly material to mitigate the challenges of the sustainable construction industry [12,13]. Indeed, the environmental impact of RSFRC has been barely studied, namely comparing to conventional Industrial Steel Fiber Reinforced Concrete (ISFRC).

In the present work, the technical and environmental benefits of using RSFRC in structural elements are assessed at material level and compared to those registered in ISFRC. The properties of the fibers and mix compositions of RSFRC and ISFRC used in this research are described in section 2. In section 3, the constitutive laws of RSFRC and ISFRC that can be used on design approaches for RSFRC/ISFRC structures were predicted. For this purpose, numerical simulations were performed for the derivation of the stress-crack width relationship, σ - ω, of RSFRC and ISFRC by inverse analysis (IA) with the experimental results presented in Frazão et al. [22], which were obtained from three-point notched beam bending tests (3PNBBT), round panel tests supported on three points (RPT-3ps) and double edge wedge splitting tests (DEWST). In section 4, the environmental impact of used RSFRC in comparison with ISFRC is analyzed by performing Life Cycle Assessment (LCA).

Additionally, in section 5, some technical and environmental benefits of using RSFRC in a structural element failing in shear was predicted. The load carrying capacity of a T-cross section steel RSFRC beam failing in shear were predicted by numerical simulation, considering the σ - ω relationship derived from 3PNBBT by IA to simulate the fracture process of the RSFRC (section 3). In addition, the environmental benefit of RSFRC in reducing the shear reinforcement was estimated by LCA.

2. Properties of the fibers and mix compositions of RSFRC and ISFRC

The RSF used in this research were recovered by a shredding process of post-consumed truck tires, which leads to a significant variability of their geometric properties. These RSF generally have irregular shape with various lengths and diameters (Fig. 1a), and most of them contain some rubber particles attached on its surface due to the shredding process (Fig. 1b). On average, followed by the standard deviation, the RSF used for RSFRC production had 20 ± 8 mm in length (l_f) defined as the distance between the outer ends of the fiber, 26 ± 10 mm in developed fiber length, 0.25 ± 0.08 mm in diameter (d_f), 110 ± 44 of aspect ratio ($\lambda = l_f/d_f$), and 2648 ± 423 MPa of average tensile strength (f_u).

For comparison purposes, it was selected for ISFRC production, one of the most commonly used hooked-end steel fibers in the ISFRC market, herein designated by ISF, with a l_f, d_f, λ and f_u of 33 mm, 0.55 mm, 60 and 1230 MPa, respectively (Fig. 1c and d). Therefore, RSFRC benefits from the higher aspect ratio and tensile strength of RSF when compared with ISF.

Recycled Steel Fiber Reinforced Concrete (RSFRC) was produced with ordinary Portland cement type CEM I 42.5R (CEM), fly ash (FA), water (W), a polycarboxylate based superplasticizer (SP) with the commercial designation MasterGlenium SKY 617, fine river sand (FS) (maximum aggregate size of 1.19 mm and fineness modulus of 1.91), coarse river sand (CS) (maximum aggregate size of 4.76 mm and fineness modulus of 3.84), crushed granite (CG1) (maximum aggregate size of 19.00 mm and fineness modulus of 7.01), and a RSF content of 1% in volume (Cf). For comparison purposes, ISFRC was produced with the same concrete matrix and equal volume of fibers. For the evaluation of the environmental impact of RSFRC in comparison to ISFRC, one reference ISFRC composition of the same strength class (C30/37) commonly used for structural applications [23], herein designated by "ISFRC_REF", was also considered with a fiber content of 1% in volume. In this reference ISFRC, crushed granite (CG2), with a maximum aggregate size
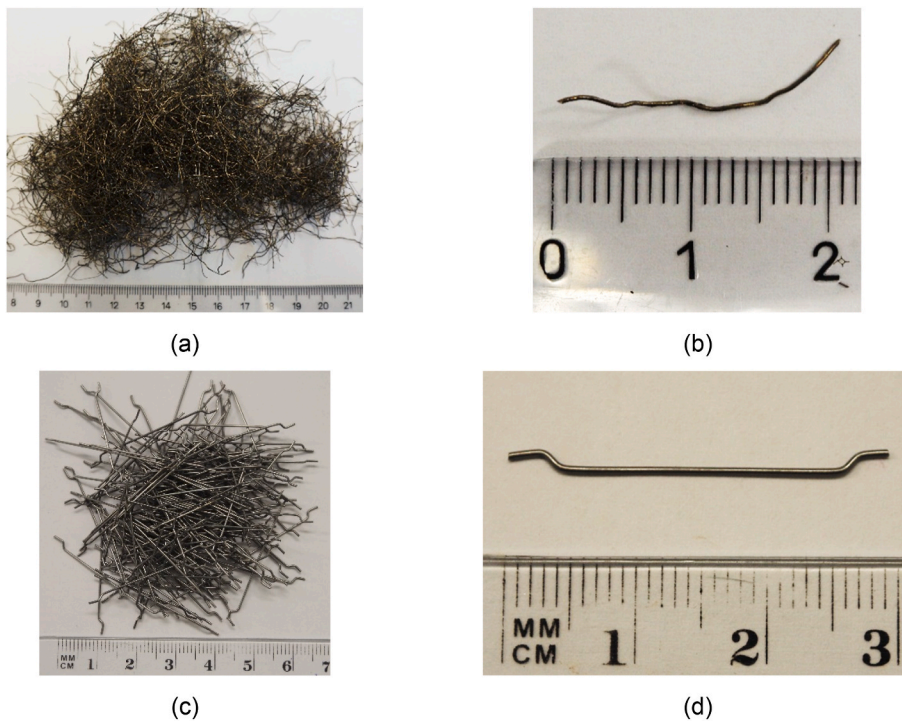
Fig. 1. Steel fibers: (a) general view of multi RSF; (b) general view of the geometry of a single RSF; (c) general view of multi ISF; (b) general view of the geometry of a single ISF.

of 25.4 mm and fineness modulus of 7.23 was also used. The mix compositions are presented in Table 1, where w/c is the effective water/cement ratio.

The mix design of RSFRC was based on the packing density optimization method suggested in Pereira [24] to achieve the optimum composition of steel fiber reinforced self-compacting concrete (SFRSCC). ISFRC was produced with the same composition for comparison purposes. A high percentage of fly ash was adopted (40% of binder volume) to improve the sustainable character of RS-FRC and to enhance the packing density and fresh concrete stability. Fly ash also improves the fresh concrete flowability, due to the spherical shape of their constituting particles that act as micro-rollers, decreasing friction and flow resistance [24]. A high dosage of superplasticizer (1.8% of cement weight) was also used to promote the dispersion and deflocculation of the fine particles in suspension, allowing the reduction of the mixing water and consequent improvement of concrete flowability and strength.

The proportions of the three types of aggregates (FS, CS and CG) were derived executing mixes of distinct quantities of each type of aggregate and weighing 5 dm^3 volume for each mixture. Taking into account the densities of FS, CS and CG particles are similar, the highest packing density was assumed to be achieved in the aggregate blend with the highest loose bulk density. Initially, only coarse sand and crushed granite were mixed. After finding the optimum relation between these two aggregates' types, the fine sand was added in distinct volumetric percentages, keeping constant the relation between the two first aggregates. An estimated portion of fibers equivalent to 76 kg of RSF per m^3 of concrete was included in every mixture in order to take into account their perturbation in the aggregate's skeleton arrangement [24]. The optimum solid skeleton composition, by volume, was obtained for 10% FS, 49.5% CS and 40.5% CG.

Finally, the concrete mixture was prepared with a paste volume of 33% and an effective w/b ratio of 0.29. The paste and water content were defined taking into account the recommendation of Pereira [24] to obtain SFRSCC with good homogeneity and cohesion, without signs of segregation. The added water was corrected by considering the aggregate's saturation degree. Table 1 summarizes the resulting RSFRC composition for 1%vol (in volume) of RSF, as presented in Frazão et al. [22]. For comparison purposes, IS-FRC was produced with 1%vol of ISF.

Table 1
Mix proportions for 1 m^3 of fiber reinforced concrete (FRC).

Concrete mixture	CEM (kg)	FA (kg)	W (L)	SP (L)	FS (kg)	CS (kg)	CG1 (kg)	CG2 (kg)	C_f (kg)	w/c
RSFRC	400	200	173	7.2	148	735	597	–	75.8	0.43
ISFRC									78.6	
ISFRC_REF	383	–	169	2.60	306	675	376	310	75	0.44

3. Post-cracking behavior of RSFRC and ISFRC

3.1. Previous experimental study

A comprehensive experimental research, involving 3PNBBT, RPT-3ps and DEWST, was carried out by Frazão et al. [22] to compare the post-cracking behavior of RSFRC and ISFRC, according to the test setups presented in Fig. 2. The 3PNBBT were conducted on notched beams with 600 mm in length and 150 × 150 mm² cross section, according to the recommendations of EN 14651:2005 + A1:2007 [25]. The RPT-3ps were performed on round panels according to the recommendations of ASTM C1550 [26]. In order to facilitate handling and placing of the specimens, smaller round panels were produced with 600 mm diameter and 60 mm thickness. According to Minelli and Plizzari [27], such reduction of the panel's diameter and thickness does not affect the scatter and repeatability of the test results when compared to the standard specimens of ASTM C1550 [26].

The DEWST were executed on notched ϕ150 × 60 mm specimens cut from molded ϕ150 × 300 mm cylinders. The DEWST test method is a combination of the methodology proposed by di Prisco et al. [28] for indirect evaluation of the mode I fracture properties of FRC and the Modified Splitting Tensile Test (MSTT) introduced by a group of researchers from the University of Minho [29], which tried to overcome the limitations of each test method. The adopted test procedures and the respective experimental results are presented in Frazão et al. [22]. From 3PNBBT and RPT-3ps, RSFRC exhibited higher flexural strength and energy absorption capacity than ISFRC of equal composition. This may be attributed to the higher aspect ratio and number of RSF for the same volume content of fibers [30]. No significant differences were found between the post-cracking tensile behavior of RSFRC and ISFRC in DEWST. In sum, the results obtained in this previous work suggest that, at least, RSFRC may have the same mechanical strength performance as ISFRC.
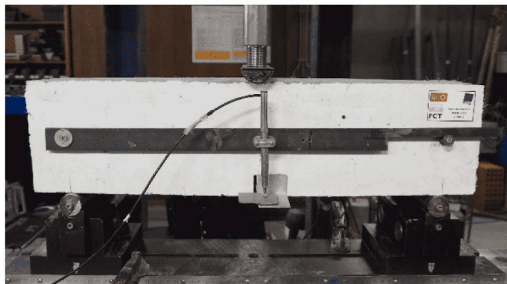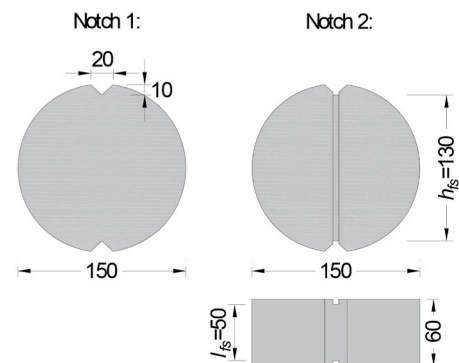

(a)

(b)
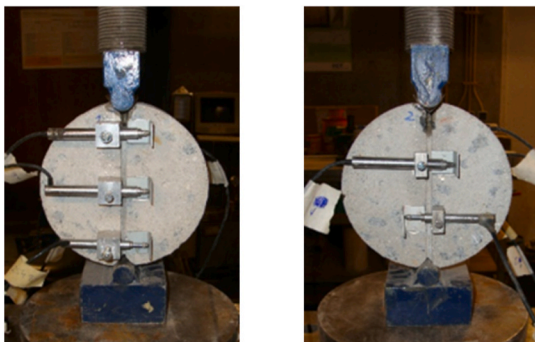
(c)

(d)

Fig. 2. Test setup of: (a) 3PNBBT; (b) RPT-3ps; (c) DEWST; (d) Schematic representation of the preparation process of DEWST specimens.

From the experimental results obtained in 3PNBBT, RPT-3ps and DEWST reported in Frazão et al. [22], in the present study the post-cracking behavior of RSFRC and ISFRC was determined by IA, as presented in the following sections.

3.2. Numerical simulations of the 3PNBBT and RPT-3ps

The IA approach proposed by Matos et al. [31] was used to predict the fracture mode I parameters of RSFRC and ISFRC by using the experimental force-deflection relationships, F - δ, obtained in 3PNBBT (in this case δ can represent not only a deflection, but also a crack mouth opening displacement (CMOD) or a crack tip opening displacement (CTOD)) and RPT-3ps. The IA tool developed by Matos et al. [31], whose corresponding software was named COFIT, includes two main modules: the Global fitting module (GFM) and the Parameter updating module (PUM). The GFM consists in a nonlinear least square fitting (NLSQ) algorithm that minimizes the error function:

$$\min \sum_{i=1}^{n} \left(F_{Exp}^{i} - F_{Num}^{i} \right)^2 \tag{1}$$

where F_{Num}^{i} and F_{Exp}^{i} are respectively the numerical and interpolated experimental forces at ith data point, and n is the number of numerical data points. The PUM consists in modifying the variables and boundaries of the tensile stress-crack width relationship (σ - ω) to be optimized, in an automatic fashion, based on the deviation error between the numerical and experimental curves corresponding to the region of each ω_i value defining the σ - ω. This aims to reduce the probability of obtaining spurious solutions and to minimize the sensibility of the solution to the initial guess of the variables provided by the user. The model is prepared to determine the optimum values of the tensile strength (f_{ct}), Young's modulus (E_c), the pair of $\omega_i, \sigma_i = \alpha_i f_{ct}$ that define the tensile behavior of a FRC (α_i - Tensile strength multiplication factor of the ith parameter), and the ultimate crack width (ω_u). According to Wang [32], the statistically representative fiber bond length is ¼ the fiber length, therefore the adopted maximum crack width for the σ - ω to be derived from COFIT was 5 mm in RSFRC and 8.25 mm in ISFRC. For a better and more efficient optimization process, COFIT allows the user to adopt different data point sampling density for a refining level according to the complexity of the experimental F - δ response. A detailed description of this IA is provided in [31].

When the IA is performed with experimental results from 3PNBBT (F - δ/CMOD/CTOD), a cross section layer model similar to the one described elsewhere [21] is adopted, where the tensile behaviour of the FRC is defined by the variables to be optimized (f_{ct}, E_c, pairs of ω_i, σ_i and ω_u). When the IA is executed with experimental results from RPT-3ps, the previous cross section layer model is integrated with the kinematics of the three rigid plates connected by the three cracks that generally form in this type of test (relative rotation of the plates in turn of the corresponding connecting crack) and also applying the principle of virtual work (external virtual work, F - $\partial\delta$, equal to the internal work due to the moment-rotation in the cracks, m - $\partial\theta$). This model is described in detail elsewhere [21].

In the present simulations, the fracture mode I propagation of RSFRC and ISFRC was simulated by a quadrilinear tensile-softening σ - ω diagram, since it was verified that its defining number of pair of ω_i, σ_i was sufficient to derive the corresponding F - δ with the aimed accuracy. The maximum force deviation error between numerical and experimental results, F_{err}, was determined according to equation (2):

$$F_{err} = \max \left(\frac{\left| F_{Num}^{i} - F_{Exp}^{i} \right|}{F_{Exp}^{\max}} \right) \tag{2}$$

where $F_{Exp}^{\max}$ is the maximum experimental force value.

3.3. Numerical simulations of the DEWST

The post-cracking behavior of RSFRC and ISFRC was also assessed by IA, fitting the average splitting tensile stress-crack width curves, $\sigma_{t,\text{split}}$ - ω, obtained in DEWST. Since the COFIT tool is limited to IA of 3PNBBT and RPT-3ps, the finite element-based program FEMIX [33] was used to simulate the numerical response by fitting, as much as possible, the experimental curves. The objective of this IA was to evaluate the fracture mode I parameters, by minimizing the equivalent fitting error, given by Equation (3).

$$err = \frac{\left| A_{Num}^{(\sigma_{t,\text{split}} - \omega)} - A_{Exp}^{(\sigma_{t,\text{split}} - \omega)} \right|}{A_{Exp}^{(\sigma_{t,\text{split}} - \omega)}} \tag{3}$$

where $A_{Num}^{(\sigma_{t,\text{split}} - \omega)}$ and $A_{Exp}^{(\sigma_{t,\text{split}} - \omega)}$ are respectively the area beneath, respectively, the experimental and numerical $\sigma_{t,\text{split}}$ - ω curves up to ultimate crack width obtained in the experimental response.

Due to the double symmetry condition of the specimen geometry (Fig. 2c), only a quarter of the specimen was modeled (Fig. 3). On both axes of symmetry, roller supports were allocated to all nodes, avoiding any displacement perpendicular to the symmetry axes. A mesh of 8-node Serendipity plane stress finite elements with 2×2 Gauss-Legendre integration points (IP) scheme was adopted for the specimen, assuming a linear elastic behavior for the material. The crack initiation and propagation were simulated by 2D line interface finite elements with 1×2 Gauss-Lobato IP, located on the symmetry axis of the specimen in the notched plane. A point load was applied orthogonally to the V-shaped groove edge, and the load process was controlled by displacement through the arc-length
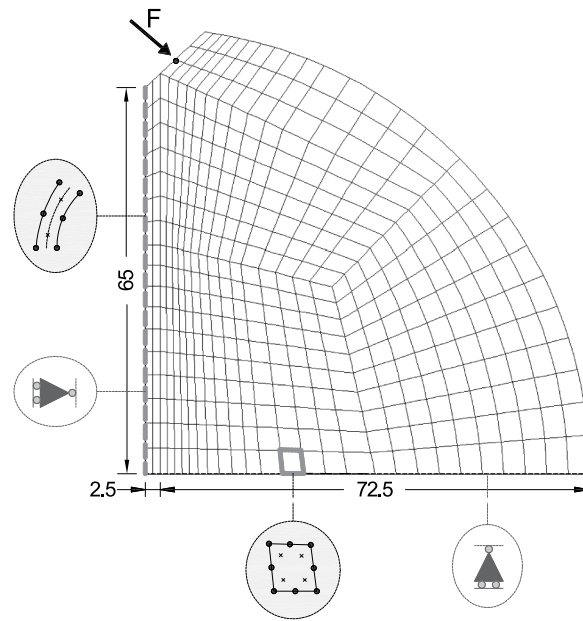
Fig. 3. Finite element mesh, support and loading conditions used in the simulation of the DEWST (units in mm).

method (Fig. 3). Fig. 3 shows the mesh used in the numerical simulations. The material properties adopted in the simulations were 0.20 for Poisson's ratio and 31.4 GPa for E_c.

The numerical values of $\sigma_{t,split}$ were determined from equation (4) proposed by di Prisco et al. [34], considering the compressive load P given by the sum of the vertical reactions at the nodes located on the horizontal symmetry axis, and h_{fs} and l_{fs} are the ligament depth (130 mm) and the thickness (50 mm) of the fracture surface (Fig. 2d).

$$\sigma_{t,split} = \frac{0.89 P}{h_{fs} \cdot l_{fs}} \tag{4}$$

The numerical values of ω correspond to the average of the horizontal displacements at the nodes located on the vertical symmetry axis. A trilinear tensile-softening σ - ω diagram was used to simulate the fracture mode I propagation of RSFRC and ISFRC. The parameters that define the shape of the σ - ω diagram, namely, the values of crack opening, ω_i, tensile stress, σ_i, and fracture energy, G_f, were obtained by performing IA with the experimental $\sigma_{t,split}$ - ω curves.

3.4. Numerical results: determination of the σ - ω by inverse analysis

Fig. 4 presents both the experimental and numerical F - δ curves of RSFRC and ISFRC notched beams at 28 days. The agreement between the numerical and the experimental curves is very good for the RSFRC and ISFRC beams, which indicates that the quadrilinear σ - ω relationship is capable of simulating accurately the post-cracking behavior of RSFRC and ISFRC.

Fig. 5 shows that the IA with the COFIT software was also capable of fitting with high accuracy the experimental F - δ relationships for RSFRC and ISFRC round panels, tested at 28 days.

Fig. 6a and b presents both the experimental and numerical $\sigma_{t,split}$ - ω curves for RSFRC and ISFRC, obtained from DEWST at 74 days. The numerical simulations were able of fitting with high accuracy the experimental results, up to the average crack width of 2.5 mm.

The obtained fracture parameters defining the shape of σ - ω diagrams, the values of F_{err} used in the numerical simulations of 3PNBBT and RPT-3ps, and the values of err obtained in DEWST are indicated in Table 2.

The fracture mode I parameters include the tensile strength, f_{ct}, the post-cracking tensile stress, σ_i, and the respective crack opening, ω_i, ultimate crack opening, ω_u, and the mode I fracture energy, G_f, as depicted in Fig. 7. The graphical representation of these σ - ω laws are presented in Fig. 8a and b for RSFRC and ISFRC.

According to Table 2 and Fig. 8a and b, the post-cracking behavior of RSFRC is at least comparable to that of ISFRC. It seems that the constitutive laws obtained from flexural tests (3PNBBT and RPT-3ps) overestimated the post-cracking tensile behavior of RSFRC and ISFRC, compared to the constitutive laws obtained from DEWST. The higher G_f values obtained from RPT-3ps are probably due to the higher percentage of fibers well oriented relative to the plane of the cracks in the round panels. The lower G_f values obtained from DEWST are probably due to an almost 3D distribution of the fibers when the $\phi 150 \times 300$ mm cylinders used to obtain the specimens tests are filled. However, higher tensile strength was predicted from DEWST than from flexural tests. This may be related to the test setup, particularly regarding the crack opening process. In the case of 3PNBBT and DEWST, the crack was forced to initiate and prop-
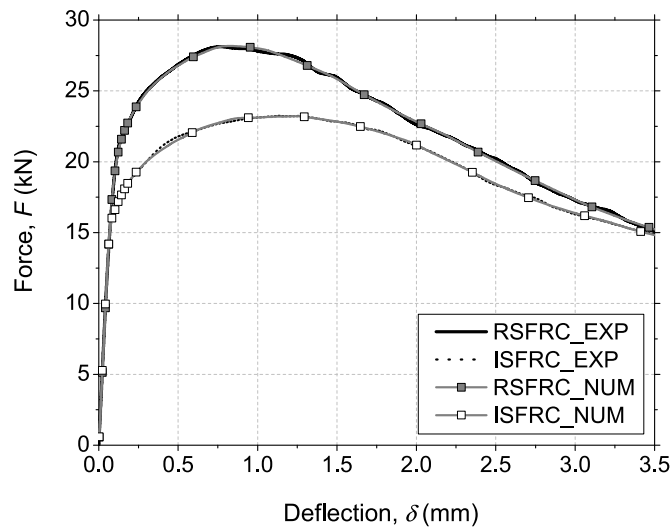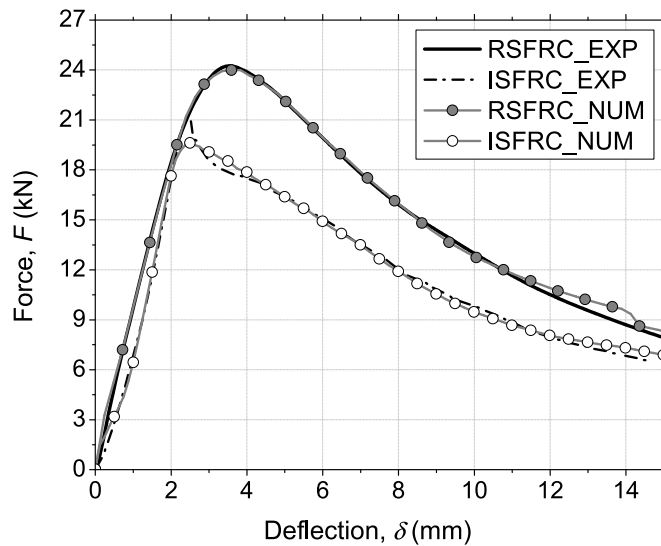
Fig. 4. Numerical simulation of the 3PNBBT.

Fig. 5. Numerical simulation of the RPT-3ps.

agate through the notched section, which may not be the weakest section. In the RPT-3ps, as no notches were implemented in the round panels, the cracks started by the least resistant sections. The difference between the f_{ct} values obtained from 3PNBBT and DEWST is related with the smaller fracture surface in DEWST compared to 3PNBBT, since forcing the location of a smaller fracture surface will have more deviant results from the reality of material weaknesses than what occurs in 3PNBBT, which has a larger fracture surface. In addition, in the DEWST, the load was applied on notched $\phi150 \times 60$ mm specimens cut orthogonally to the casting direction. In this case, the degree of consolidation of the FRC, the quality of interfacial transition zone between aggregates and cementitious matrix subjected to tensile stresses, and the intensity and orientation of the microcracks that develop at the aggregate-paste interface during curing of the three types of specimens justify the higher tensile strength of FRC obtained in DEWST (Fig. 9).

After performing the DEWST, the fiber distribution was evaluated by counting the number of effective fibers crossing the fracture surface. A fiber was considered effective when its length was visible, assuming that has failed by pull-out. On average, 4.42 fibers/cm² (CoV = 28%) and 1.60 fibers/cm² (CoV = 20%) were determined in the crack surface of RSFRC and ISFRC, respectively. The lower number of fibers in ISFRC specimens is attributed to the lower aspect ratio and higher length of ISF, resulting in fewer fibers for the same percentage of fibers per concrete volume. The variability of the fibers amount across the crack surface was slightly higher in RSFRC than in ISFRC. This is attributed to the irregular length and longitudinal configuration of RSF that make it more difficult to ensure a homogeneous distribution of these fibers in the matrix. However, as found in Fig. 8a and b, the fiber distribution in RSFRC did not significantly influence the indirect tensile strength and post-cracking behavior of concrete, compared to ISFRC. The larger number of RSF may have compensated the detrimental impact of this higher non-uniform fiber distribution.
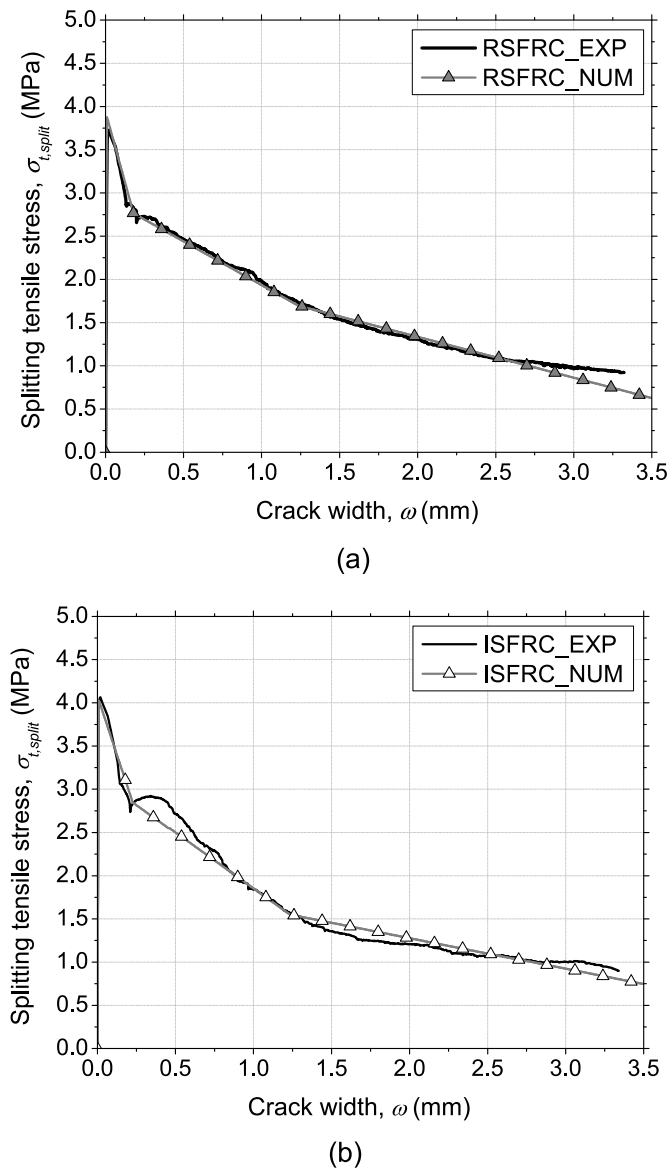
Fig. 6. Numerical simulation of the DEWST: (a) RSFRC; (b) ISFRC.

Table 2
Parameters of the σ - ω relationship obtained by IA of the 3PNBBT, RPT-3ps and DEWST.

Test setup	Type of FRC	f_{ct}(MPa)	σ_1(MPa)	σ_2(MPa)	σ_3(MPa)	ω_1(mm)	ω_2(mm)	ω_3(mm)	ω_u(mm)	G_f(N/mm)	F_{err}(%)	err(%)
3PNBBT	RSFRC	3.67	1.03	0.68	0.36	1.16	1.97	3.72	5.00	4.56	1.20	–
	ISFRC	3.41	1.18	0.32	0.15	1.05	3.83	6.21	8.25	5.21	1.12	–
RPT-3ps	RSFRC	3.03	2.35	0.77	0.75	1.22	2.84	4.38	5.00	7.22	4.67	–
	ISFRC	2.03	0.72	0.55	0.48	3.09	3.14	5.16	8.25	6.07	7.58	–
DEWST	RSFRC	4.50	3.15	1.94	–	0.06	0.41	–	1.60	2.27	–	1.30
	ISFRC	4.80	3.36	1.82	–	0.08	0.41	–	1.60	2.49	–	0.88

4. Environmental impact of RSFRC and ISFRC: Life Cycle Assessment

4.1. Goal and scope definition

In this research, the LCA methodology was used to assess the environmental impact of RSFRC in comparison to ISFRC based on ISO standards 14,040–44:2006 [35,36], and on EN 15804:2012 + A1 [37]. The goal is to evaluate the environmental sustainability of the developed concrete reinforced with 1% in volume of RSF retrieved from end-of-life tires, in comparison with different concretes
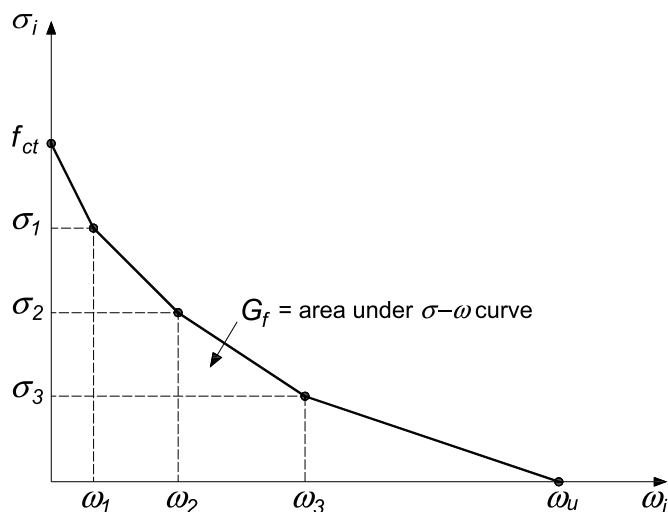
Fig. 7. Quadrilinear σ - ω relationship for modeling fracture mode I.

reinforced with ISF, as presented in Table 1. To this end, firstly, emissions were evaluated to produce 1 ton of each raw material from a cradle to gate perspective. Then, the environmental burdens of RSFRC, ISFRC and ISFRC_REF were evaluated, considering the mix proportions for 1 m³ of concrete presented in Table 1.

The system boundary was limited at raw material extraction and processing since the transport of raw materials and the manufacturing process of the concretes were considered identical for the three concrete mixtures (see Fig. 10) and therefore will have no impact on the main purpose of the analysis. Actually, according to Filippo et al. [38], the raw material stage represents approximately 94% of the concrete environmental impact at the product stage. As reference for the LCA method, some detailed LCA of similar materials are published in [13,39].

The selection of the functional unit plays a relevant role in the performance of the environmental assessment, especially when products are compared. The functional units selected were a unit of concrete volume (1 m³) and a functional performance unit relevant of the FRC properties, 1 MPa of indirect tensile strength [22]. According to Damineli et al. [40], using a performance indicator as a functional unit allows avoiding the distinction between a material scale, where impacts are expressed in kg or m³, and a structural scale, where the effective volume to provide the function is used. In this case, the efficiency and the environmental benefits of concretes with different performances are better comparable.

4.2. Life cycle inventory (LCI)

This stage of LCA involves the input and output data collection of the life cycle phases considered. According to Muralikrishna and Manickam [41], two types of data are distinguished, foreground and background data. Foreground data refers to very specific data that generally come from industries, and results in a more reliable LCI. However, this is not always provided by the companies due to confidentiality issues. The environmental product declarations (EPD) are another source to obtain high quality and suitable data. In addition, the "cradle to gate" assessments are sometimes the basis for EPD [41], which have identical system boundary of LCA. Background data is obtained from generic materials, energy, transport and waste management systems, typically found in databases and literature.

In this study, different sources have been selected for the data collection, in the following order of priority: data provided by the suppliers; EPD; databases; and scientific papers related to the material or process under study. The input data for the LCI of RSF and ISF was provided by the suppliers (for confidentiality reasons, this data is not presented in this paper), namely regarding the energy and material consumptions, waste generation and production and transport emissions.

The environmental impact data of cement was obtained from the European Life Cycle Database (ELCD) version 3.2 [42]. The environmental impact of fly ash and superplasticizer was obtained from International EPD [43,44]. The LCA of the aggregates and water was based on scientific papers published in literature, since the EPD of these materials were not available. The environmental impact of fine and coarse river sand and water was obtained using site-specific data adapted from a research study of Kurda et al. [45]. The LCA data of crushed granites was adapted by a site-specific data from a research study of Braga et al. [46], in Portuguese companies.

The data on the background processes (electricity and transport) were collected from databases, particularly from the ELCD. The primary LCI data were collected attending to geographic, temporal, and technological representativity.

4.3. Life cycle impact assessment

The life cycle impact was assessed through the analysis the environmental impact categories required for EPD in EN 15804:2012 + A1 [37]: Global warming potential (GWP) – Climate change, ozone depletion potential (ODP), photochemical ozone creation potential (POCP), acidification potential of land and water (AP), eutrophication potential (EP), abiotic depletion potential (two components: ADP - elements, ultimate reserves and ADP - fossil fuels), and two environmental parameters to quantify the energy

(a)

(b)
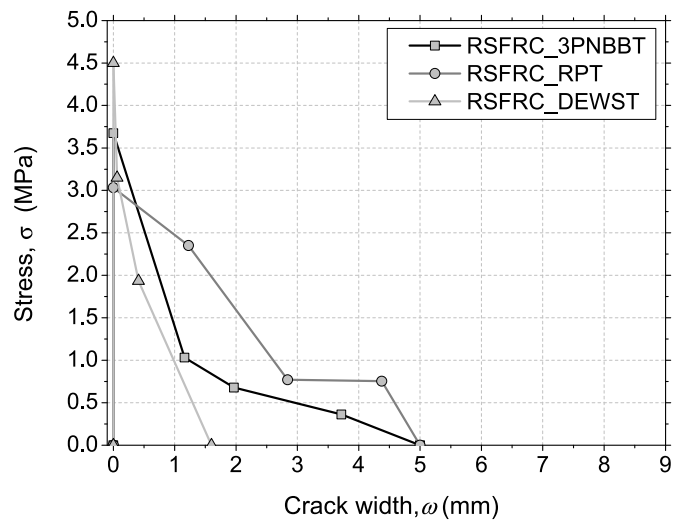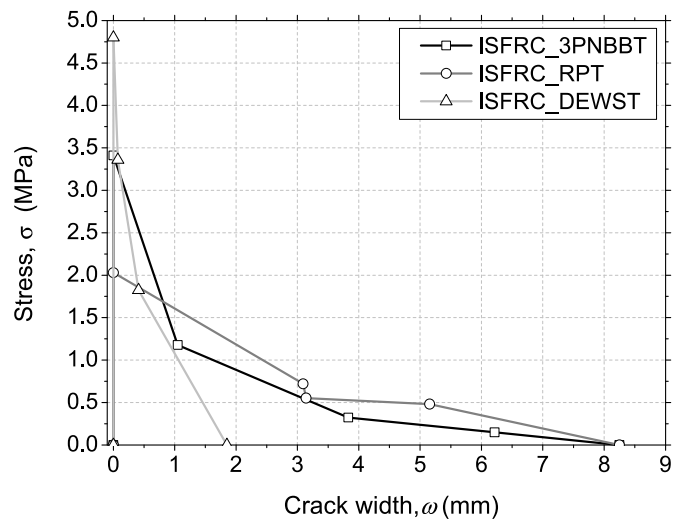
Fig. 8. σ - ω relationships obtained by IA from: (a) RSFRC; (b) ISFRC.

use, namely, total non-renewable primary energy consumption (PE-NRe), and total renewable primary energy consumption (PE-Re). The first six impact categories were analyzed according to the method developed by the Institute of Environmental Sciences (CML - Centrum voor Milieuwetenschappen in Leiden) of the University of Leiden (Netherlands), one of the most commonly applied in practice [47], as well as the method required for the EPD development. The last two impact categories (PE-NRe and PE-Re) were analyzed according to the Cumulative Energy Demand (CED) Method. This selection was motivated by its widespread use and wide acceptance for the evaluation of building products. In addition, the evaluation according to the EPD allows the use of data for the LCI and facilitates comparison with other analyses as long as they have been performed under the same assumptions and system limits. As the "cradle to gate" assessments are sometimes the basis for EPD [41], the environmental impact was directly collected from the EPD. The software OpenLCA 1.7 was used to calculate the environmental impact of the RSF, ISF and cement.

In Tables 3 and 4, the environmental impact to produce 1 ton of each raw material is presented.

After obtaining the environmental impact of each raw material, the environmental impact of FRC per m³ (Tables 5 and 6). was modeled by multiplying the environmental impacts of each component (Tables 3 and 4) by the quantities of the corresponding FRC mixes (Table 1).
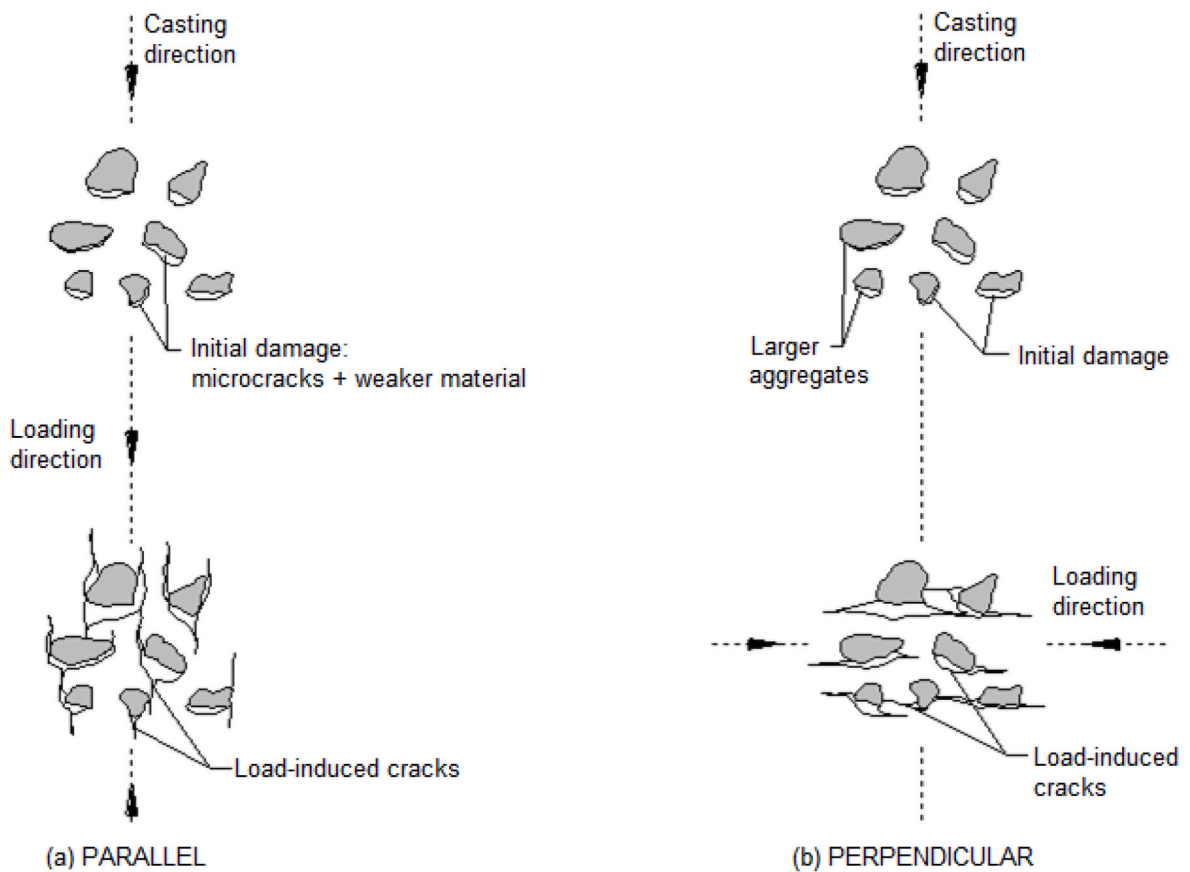
Fig. 9. Propagation of microcracks for loading in the parallel and orthogonal direction to the casting direction.
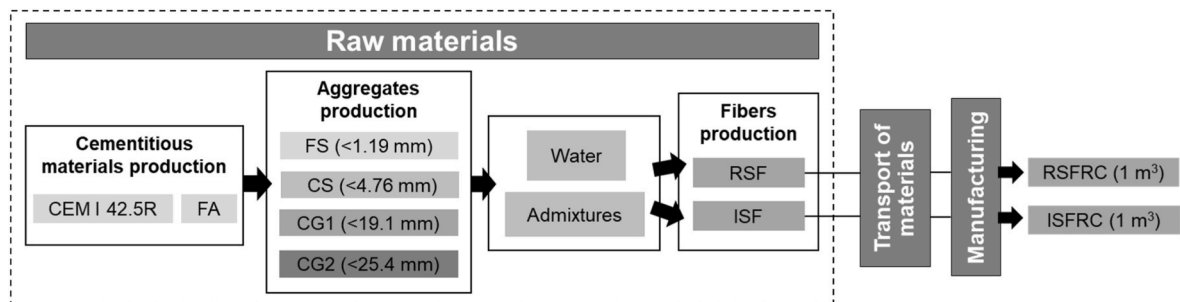

Fig. 10. System boundaries considered for ISFRC and RSFRC production.

4.4. Environmental impact results

The LCA of the three fiber reinforced concretes considered in Table 1 was assessed by analyzing the above-mentioned environmental impact categories, as presented in Tables 5 and 6.

As expected, for 1 m^3 of concrete, the RSFRC showed lower environmental impact than ISFRC with the same composition, especially regarding the environmental impact categories of GWP, PE-Re, PE-NRe, POCP and ADP-Fossil fuels, with an impact reduction of 17%, 20%, 28%, 34% and 34%, respectively. Comparing to "commercial mixture" of ISFRC, the RSFRC showed lower environmental impact than ISFRC with similar fiber volume content (ISFRC_REF).

The results obtained for each environmental impact category, considering the functional unit of 1 MPa of indirect tensile strength are presented in Tables 7 and 8. These results were obtained by dividing the impact values presented in Tables 5 and 6 for RSFRC and ISFRC by the maximum splitting tensile strength obtained for these concretes, as reported in Frazão et al. [22], namely 3.74 MPa and 4.10 MPa for RSFRC and ISFRC, respectively.

Table 3
Baseline CML method results for raw materials (for 1 ton).

Raw Materials	GWP kg CO_2 - eq.	ODP kg CFC11 - eq.	POCPkg ethen - eq.	AP kg SO_2 - eq.	EPkg PO_4^{-3} – eq.	ADP Elementskg Sb - eq.	Fossil fuels MJ
RSF	54.74	8.63×10^{-6}	1.62×10^{-2}	3.27×10^{-1}	1.72×10^{-2}	1.36×10^{-6}	641.99
ISF	1095.88	7.97×10^{-7}	5.00×10^{-1}	2.98	3.07×10^{-1}	0	11370.00
CEM	903.23	4.37×10^{-5}	1.66×10^{-1}	2.21	2.59×10^{-1}	1.43×10^{-5}	3472.05
FA	0.20	1.21×10^{-13}	$- 1.36 \times 10^{-5}$	3.84×10^{-4}	6.50×10^{-5}	1.72×10^{-9}	2.08
W	0.26	3.01×10^{-8}	5.88×10^{-5}	1.31×10^{-3}	7.28×10^{-4}	5.83×10^{-7}	–
SP	1880.00	2.30×10^{-7}	2.12×10^{-1}	2.92	1.03	1.10×10^{-3}	29100.00
FS	1.73	0	1.25×10^{-4}	9.58×10^{-3}	2.49×10^{-3}	0	–
CS	4.56	2.33×10^{-7}	1.33×10^{-3}	6.22×10^{-2}	1.37×10^{-2}	6.56×10^{-9}	–
CG	24.40	2.43×10^{-7}	7.83×10^{-3}	1.44×10^{-1}	3.18×10^{-2}	1.09×10^{-6}	–

Table 4
Cumulative Energy Demand (CED) results for raw materials (for 1 ton).

Raw Materials	PE-NRe MJ	PE-Re MJ
RSF	990.72	15.27
ISF	12100.00	219.28
CEM	4111.57	132.20
FA	2.08	2.99×10^{-2}
W	5.08	6.83×10^{-1}
SP	31400.00	1510.00
FS	17.60	0
CS	62.30	0
CG	344.00	3.81×10^{-1}

Table 5
Baseline CML method results for 1 m³ of concrete.

Concrete	GWP kg CO_2 - eq.	ODP kg CFC11 - eq.	POCPkg ethen - eq.	AP kg SO_2 - eq.	EPkg PO_4^{-3} – eq.	ADP Elementskg Sb - eq.	Elementskg Sb - eq.
RSFRC	397.24	1.85×10^{-5}	7.47×10^{-2}	1.06	1.42×10^{-1}	1.45×10^{-5}	1647.42
ISFRC	479.22	1.79×10^{-5}	1.13×10^{-1}	1.27	1.65×10^{-1}	1.44×10^{-5}	2492.44
ISFRC_REF	453.41	1.71×10^{-5}	1.08×10^{-1}	1.22	1.57×10^{-1}	9.18×10^{-6}	2258.21

Table 6
Cumulative Energy Demand (CED) results for 1 m³ of concrete.

Concrete	PE-NRe MJ	PE-Re MJ
RSFRC	2200.86	65.26
ISFRC	3076.83	81.34
ISFRC_REF	2848.15	71.38

Table 7
Baseline CML method results for 1 MPa of indirect tensile strength.

Concrete	GWP kg CO_2 - eq.	ODP kg CFC11 - eq.	POCPkg ethen - eq.	AP kg SO_2 - eq.	EPkg PO_4^{-3} – eq.	ADP Elementskg Sb - eq.	Fossil fuels MJ
RSFRC	106.21	4.94×10^{-6}	2.00×10^{-2}	0.39	6.21×10^{-2}	3.87×10^{-6}	440.49
ISFRC	116.88	4.36×10^{-6}	2.75×10^{-2}	0.41	6.22×10^{-2}	3.51×10^{-6}	607.91

Table 8
Cumulative Energy Demand (CED) results for 1 MPa of indirect tensile strength.

Concrete	PE-NRe MJ	PE-Re MJ
RSFRC	588.47	17.45
ISFRC	750.45	19.84

In general, for 1 MPa of indirect tensile strength, the RSFRC showed similar to lower environmental impact than ISFRC, for the impact categories obtained by the baseline CML method (Table 7). Regarding the results obtained for the cumulative energy demand, the RSFRC showed an PE-NRe impact lower than ISFRC. The RSFRC had a PE-Re impact comparable to that of ISFRC.

4.4.1. Global warming potential (GWP)

Also known as "Greenhouse effect", the GWP is a measure of the amount of the "greenhouse gases" emitted to the atmosphere relative to carbon dioxide. At a global scale, the heat trapped by the greenhouse gases results in an increase of the global medium temperature, which further rises with the increase of the concentration of these gases. This global warming may result in several climate changes with significant influence in the ecosystems and human health, since it is responsible for several environmental impacts, such as polar melting, soil moisture loss, longer seasons, forest loss/change, and change in wind and ocean patterns [48,49].

Cement was the component that contributed the most to the global warming impact, being responsible for more than 75% of the GWP impact of analyzed concretes, as observed in Fig. 11. The ISF also contributed to this impact (about 18%). The remaining concrete ingredients had a negligible effect in the GWP impact (maximum 8%). The RSFRC presented lower GWP impact than ISFRC with the same concrete matrix and fiber content (17% lower than ISFRC and 12% lower than ISFRC_REF).

4.4.2. Ozone depletion potential

The ozone depletion potential (ODP) gives the relative amount of degradation to the ozone layer in the atmosphere by Halocarbons (HCFCs). The depletion of the stratospheric ozone layer increases the vulnerability of the Earth's surface to the ultraviolet radiation, with a negative effect in the ecosystems and human health [50]. However, as the HCFCs were already banned in Europe and in USA, the analysis of this environmental category is just indicative and does not have a significant influence on the assessment of the environmental sustainability [49].

The main contributor to the ODP impact was also the cement, representing 95% of the total ODP impact produced by the RSFRC and 98% of the total ODP impact produced by the remaining concretes (Fig. 12). The production of RSF from end-of-life tire recycling
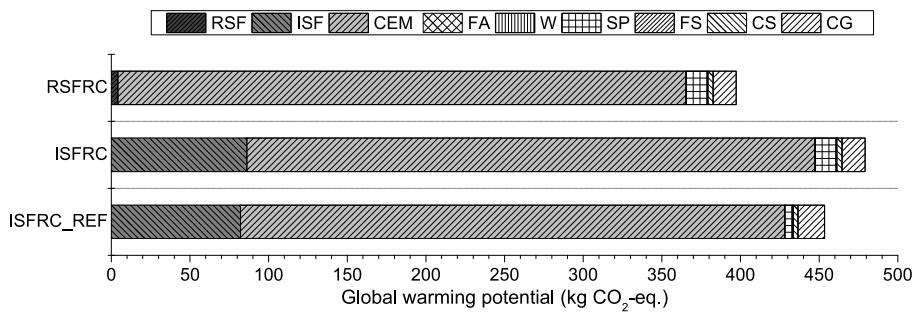

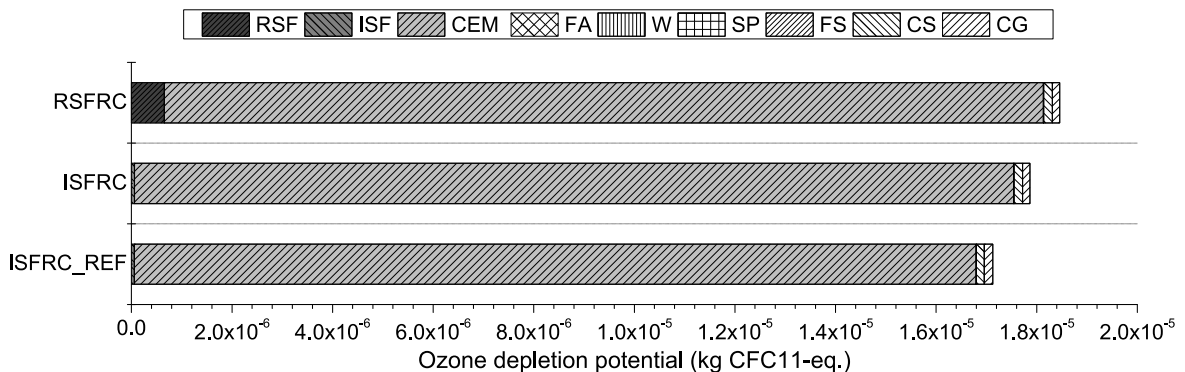**Fig. 11.** Global warming potential impact.

Fig. 12. Ozone depletion potential impact.

had a higher ODP impact than the ISF production. Therefore, the RSFRC showed slightly higher ODP impact than ISFRC (about 3%). Consequently, the incorporation of RSF in FRC, as alternative to ISF, is not beneficial regarding this environmental impact category.

4.4.3. Photochemical ozone creation potential

Photochemical ozone creation potential (POCP), also known as summer smog, quantifies the relative abilities of volatile organic compounds to produce ground level ozone. The concentrations of ozone are higher in the summer and, due to its toxic nature, can directly affect human health and ecosystems disruption [48].

According to Fig. 13, cement and ISF were the components that mostly contributed to the POCP impact in the concretes analyzed, increasing the concentration of ozone at the ground level. Cement was responsible for 89% of the POCP impact in RSFRC and from 59% in the ISFRC mixtures. The production of ISF had a significant contribution to POCP impact when used at high content (about 35% in ISFRC and ISFRC_REF).

4.4.4. Acidification potential of land and water

Acidification Potential (AP) is a consequence of acids being emitted to the atmosphere and subsequently deposited in surface soils and waters. The main gases responsible for acidification are produced by the combustion of fossil fuels, and cause a wide range of impacts on soil, ground and surface water, organisms, ecosystems and materials [46,49].

Fig. 14 shows the total impact of the analyzed concretes in the AP impact category. The AP impact was essentially influenced by cement and ISF. In RSFRC, the impact of cement was around 83% while in ISFRC mixtures was around 70% of the total. The production of ISF had a significant contribution to AP impact (about 18% in ISFRC and ISFRC_REF). For this reason, the total AP impact was lower in RSFRC compared to ISFRC.

4.4.5. Eutrophication potential

Eutrophication is often induced by the discharge of mainly nitrogen and phosphorus from polluting emissions, wastewater and fertilizers, originating the enrichment with minerals and nutrients of a body of water (aquatic environment), which induce excessive growth of algae and plants. This process may result in oxygen depletion of the water body and causes the contamination of plants and groundwater in terrestrial eutrophication [46].

Fig. 15 presents the impacts produced by each concrete in the Eutrophication Potential (EP) environmental impact category. Similar to AP impact, the EP impact was mainly influenced by cement (73% in RSFRC/ISFRC and 63% in ISFRC_REF). The total EP
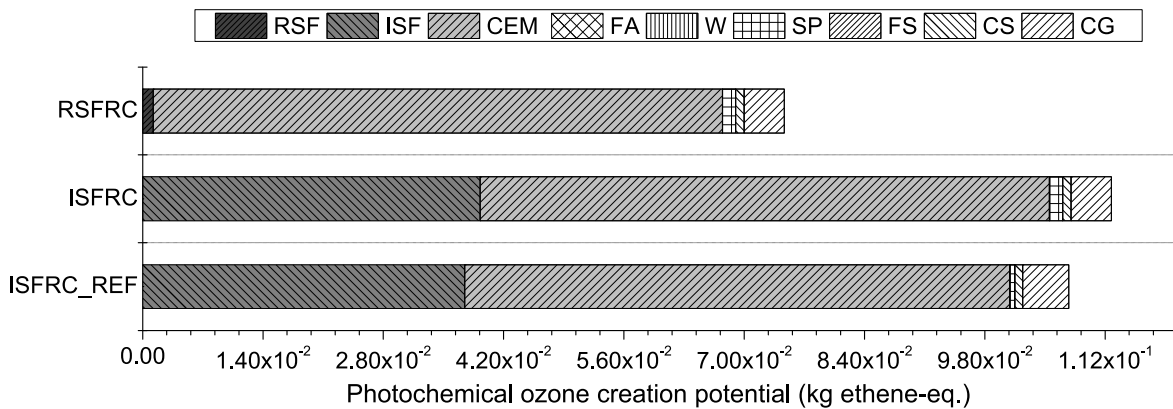

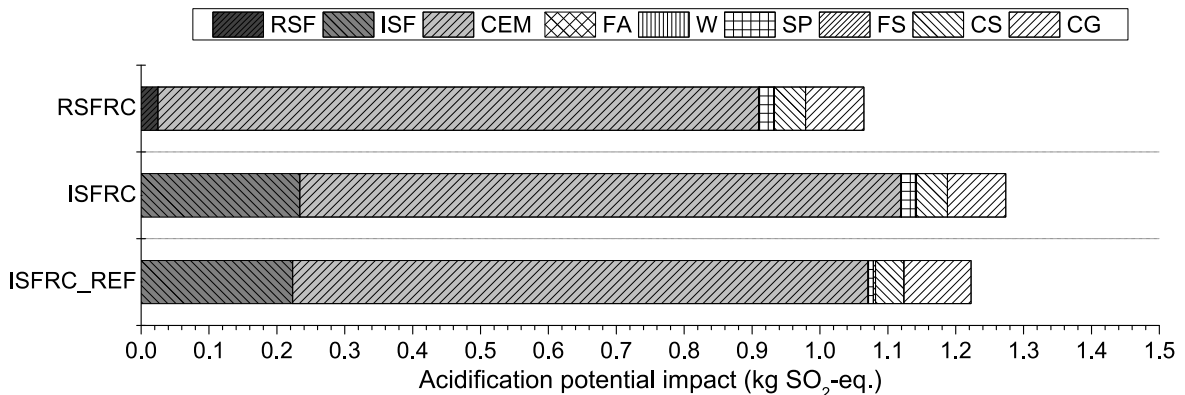**Fig. 13.** Photochemical ozone creation potential impact.

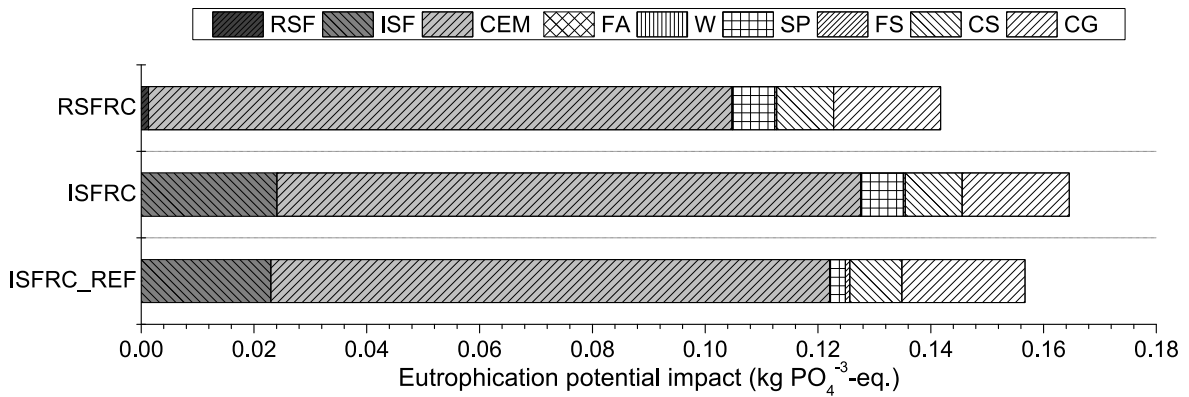**Fig. 14.** Acidification potential impact.

Fig. 15. Eutrophication potential impact.

impact was lower in RSFRC compared to ISFRC due to the higher influence of ISF production compared to RSF (about 15% in ISFRC and ISFRC_REF).

4.4.6. Abiotic depletion potential

Abiotic depletion potential (ADP) refers to the depletion of nonliving (abiotic) natural resources, such as minerals and fossil fuels. This environmental category is divided in two components: a material component, ADP – Elements for non-fossil resources (in kg Sb equivalent) and an energy component, ADP – Fossil fuels for fossil resources (in MJ).

4.4.6.1. ADP-elements. Cement and superplasticizer were the constituents with higher influence on this ADP impact category (Fig. 16). The cement and the superplasticizer were responsible for about 40% and 55%, respectively, of the total impacts of RSFRC and ISFRC. A lower impact was obtained in ISFRC_REF, due to the lower content of superplasticizer (the SP was responsible for 31% of the total impacts in ISFRC_REF). The RSF production affected more the ADP - Elements impact category, however, it only caused a slight increase of the total impact of RSFRC compared to ISFRC (1%).

4.4.6.2. ADP-fossil fuels. In this environmental impact category, the concretes' constituents that most contribute were cement and ISF (Fig. 17). The cement was responsible for 56%–84% of the total impact. The ISF production in a volume content of 1% greatly contributes to this environmental impact category compared to RSF production, being about 36% in ISFRC and 38% in ISFRC_REF. The RSFRC had a total ADP-fossil fuels impact 34% lower than ISFRC and 27% lower than ISFRC_REF.

4.4.7. Use of non-renewable primary energy resources

The non-renewable primary energy (PE-NRe) is produced by resources that cannot be replenished on human time scale [37]. Fig. 18 presents the PE-NRe impacts produced by each analyzed concrete composition. Cement was responsible for 53%–75% of the total PE-NRe impacts. The production of ISFRC with 1% of ISF in concrete volume had a significant contribution for the total PE-NRe impact of ISFRC (around 32%), similar to the influence of ISF in the previous environmental impact categories, GWP, POCP and ADP – Fossil fuels. The amounts of superplasticizer and crushed granite were the main responsible for the remaining PE-NRe impact of concretes. The RSFRC showed lower PE-NRe impact than ISFRC (28%) and ISFRC_REF (23%).
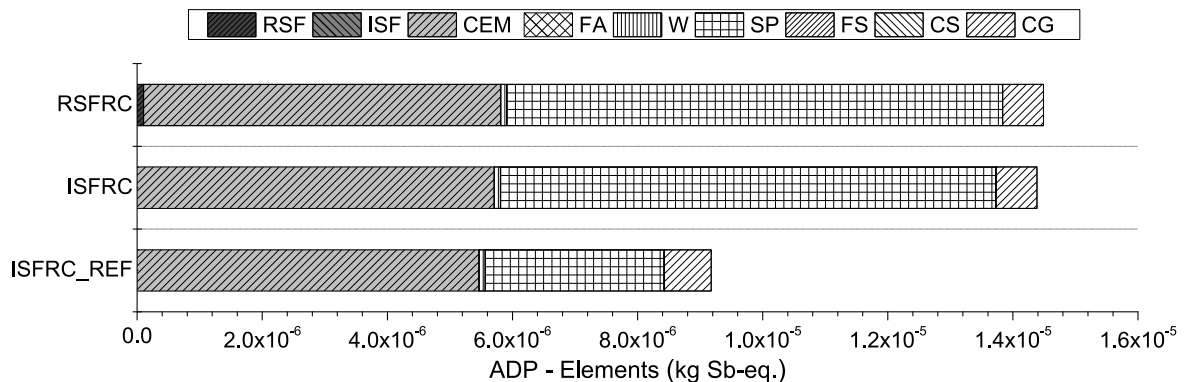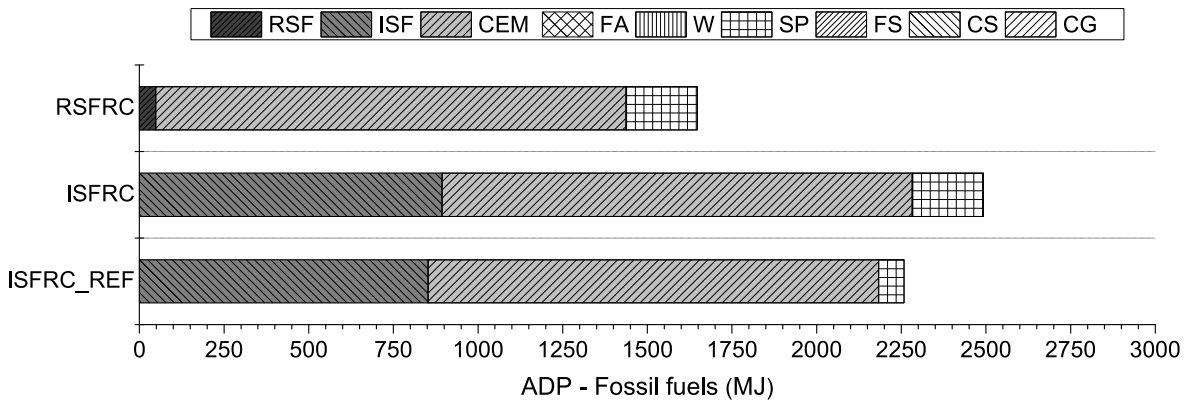

Fig. 16. ADP – Elements impact.

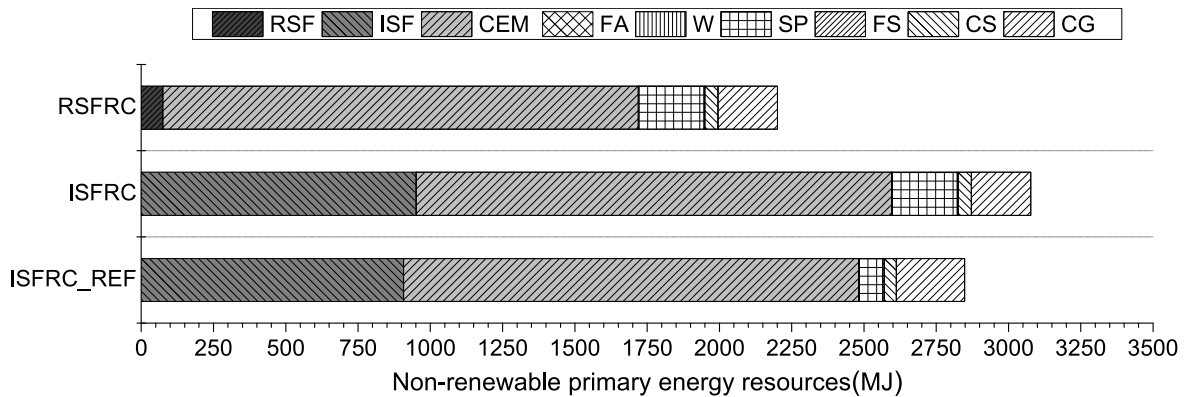**Fig. 17.** ADP – Fossil fuels impact.

Fig. 18. Non-renewable primary energy (PE-NRe) resources impact (in MJ).

4.4.8. Use of renewable primary energy resources

The renewable primary energy (PE-Re) comes from renewable sources (typically non-fossil sources) that grown naturally, are replenished or cleansed on a human time scale [37]. The ISF, cement and superplasticizer productions were the components that most influenced the PE-Re impact, as observed in Fig. 19. The ISF production is responsible for more than 20% of the total PE-Re impact in ISFRC and ISFRC_REF. The cement was the component with more renewable energy consumption (from 65% to 81% of the total renewable energy spent). The superplasticizer was responsible for 17% of the total PE-Re impact in RSFRC and for 13% in ISFRC. The RSFRC showed less than 24% or 9% energy consumption than ISFRC and ISFRC_REF, respectively.
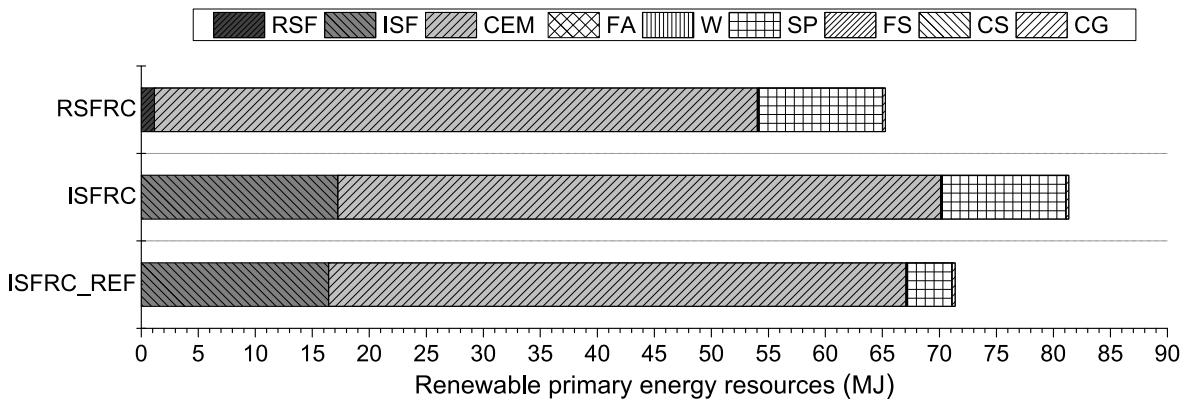

Fig. 19. Renewable primary energy (PE-Re) resources impact (in MJ).

5. Prediction of mechanical performance and environmental benefits of RSFRC beams failing in shear

For assessing the potentialities of the RSFRC in structural applications, and evaluating the corresponding environmental benefits, the results obtained in a blind simulation competition (BSC) carried out by the *fib* WG 2.4.1 were used. In this competition, two twin T cross sections beams, whose geometry, reinforcement details, loading and support conditions are presented in Fig. 20, were experimentally tested. These beams were cast with an ISFRC prepared for this competition, where steel fibers were used to completely eliminate the steel stirrups of the shortest span length (associated with the highest shear forces). The objective of this BSC was essentially to appraise the predictive performance of existing FEM-based computer programs in terms of load-deflection, strain-deflection and failure mode. The description of this BSC and the relevant obtained results are available elsewhere [51].

In the present section the behavior of this beam is also simulated, but now using the σ - ω relationship determined in section 3.4 with the COFIT applied to the results from the 3PNBBT prepared with RSFRC, since the fiber distribution in this type of specimens should be more representative of the one in the full-scale tested beams [51]. After numerically determining the beam's load carrying capacity, the number of conventional steel stirrups that assure the beam's shear capacity is determined according to the EC2 [52] recommendations, and the environmental benefits of using RSFRC is estimated. The 2D multidirectional fixed smeared crack model available in the FEM-based software FEMIX [33], already used by the last author of the present publication in the indicated BSC, was also adopted in the present simulations. This model is described elsewhere [53], and the main difference regarding both simulations is almost resumed to the σ - ω relationship.

The model of the beam was formed with 4800 plane stress 4-noded elements with 2×2 Gauss-Legendre integration points (IP) scheme to simulate the concrete elements, 1530 2-noded cables with 2 Gauss-Legendre IP scheme to simulate the steel reinforcement bars (perfect bond conditions were assumed for the top longitudinal reinforcements and stirrups), and 230 4-noded interface elements with 2 Gauss-Lobato IP scheme to simulate the bond interface of the bottom longitudinal steel bars (Fig. 21). The thickness of the plane stress elements was considered according to the cross-section of the beam (400 mm for the flange and 200 m for the web), and the area of the cables are defined according to the sum of the nominal cross-sectional area of the steel bars positioned at each level of the cross-section.

For the main parameters of the used MDFSCM applied to the RSFRC (NLMM104), the following values were adopted: $E_c = 24.31$ GPa, $f_c = 39.42$ MPa, Poisson ratio (ν) of 0.20. A linear-elastic behavior was assumed for the RSFRC in compression and σ - ω was determined from the IA with COFIT (Fig. 8a and Table 2 regarding RSFRC and 3PNBBT).

To simulate the shear stress transfer, the shear softening diagram represented in Fig. 22 was adopted [54], whose model parameters are defined based on the experience of the CiviTest's team on the material nonlinear analysis of reinforced FRC (R/FRC) structures failing in shear. For each integration point, a maximum of 2 cracks can be formed, with a threshold angle of 30°. To ensure that the results are independent of the finite element (FE) mesh refinement, a crack bandwidth equal to the square root of the finite element's area was considered. Preliminary analysis on the influence of the FE mesh refinement was performed and the adopted refinement assured proper compromise between level of accuracy on the predictions and computing time.

The stress-strain diagram for simulating the behavior of the steel reinforcements and the corresponding defining parameters are presented in Fig. 23.
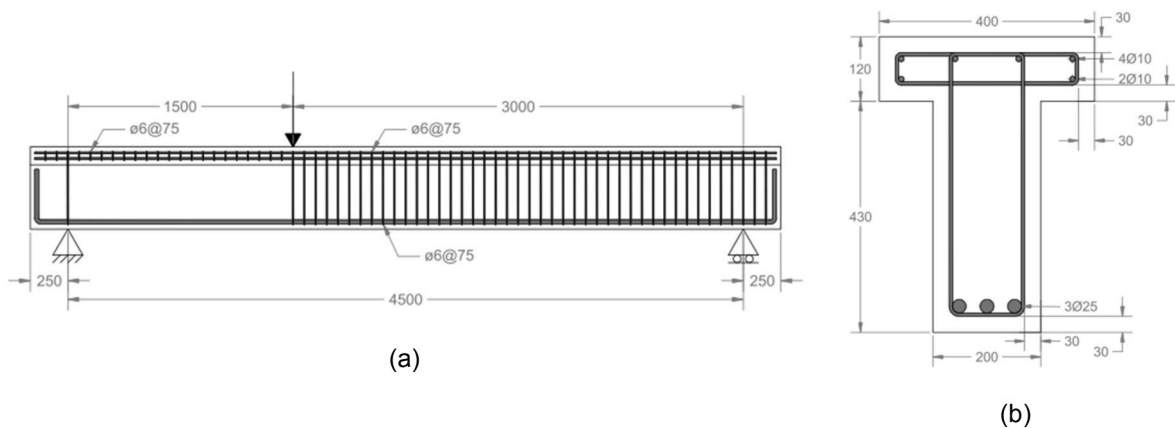

Fig. 20. Geometry of the beam: (a) Cross-section, and (b) Longitudinal view (dimensions in mm) [51].
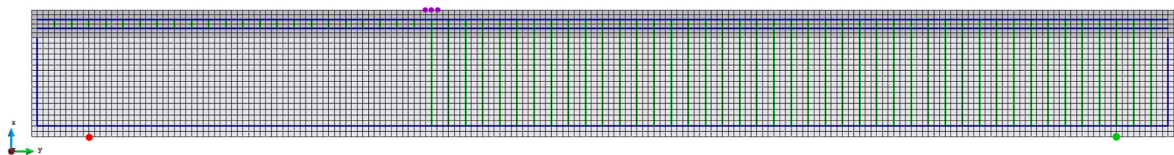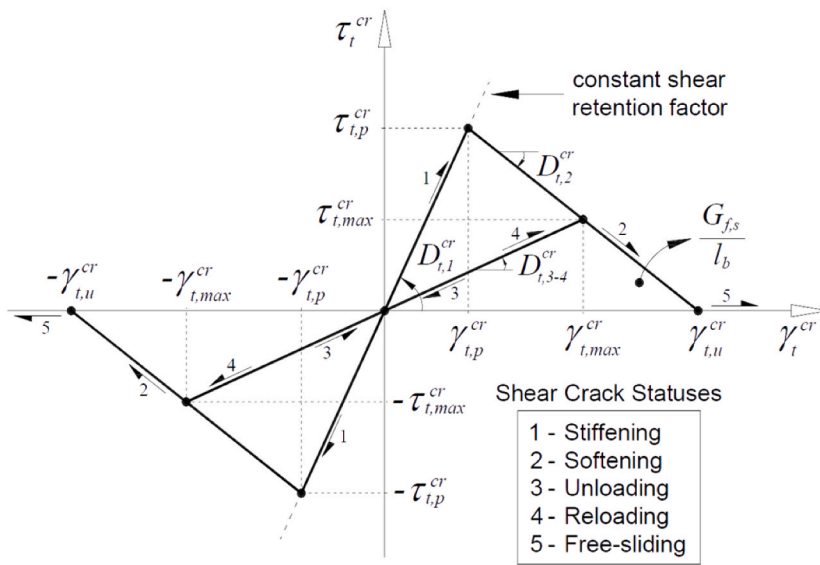

Fig. 21. Finite element reference mesh (Legend: gray elements – SFRC; blue lines – longitudinal steel bars; green lines – transversal steel bars; red dot – nodes with null displacements in y and x-axis; green dot – nodes with null displacements in y-axis; magenta dot – nodes with point loads).
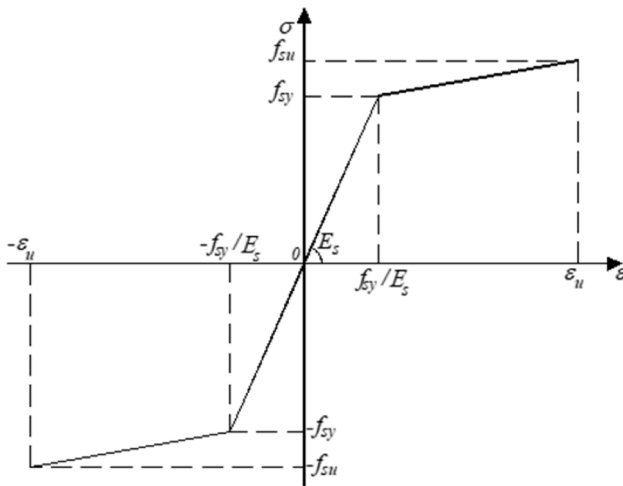
$$D_{t,1}^{cr} = \frac{\beta}{1-\beta} G_c$$

$$G_c = \frac{E_c}{2(1+\nu)}$$

$\tau_{t,p}^{cr}$	1.0 MPa
β	0.5
$G_{f,s}$	0.75 N/mm

Fig. 22. Shear softening diagram and parameters.

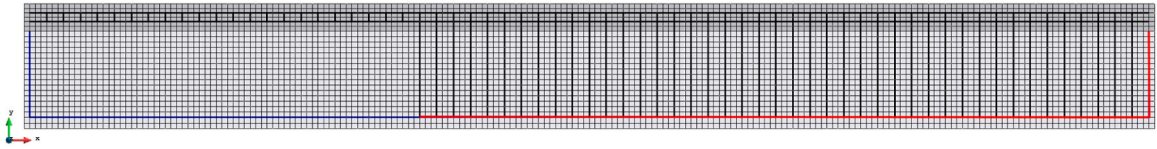|	Bar diameter (mm)		
	6	10	25
E_s (GPa)	200	200	200
f_{sy} (MPa)	527	538	557
f_{su} (MPa)	700	696	678
ε_{su} (−)	0.075	0.09	0.10

Fig. 23. Steel nonlinear material model diagram and parameters.

The bond versus slip law adopted for modeling the interface between the bottom longitudinal steel bars and surrounding RSFRC is presented in Fig. 24. Two different bond-slip relationships were considered in order to take into account the different confinement conditions of these reinforcements in the two shear spans of the beam (the steel stirrups provide higher confinement). The interface parameters presented in Fig. 24 are based on the fib Model Code 2010 [55] provisions.
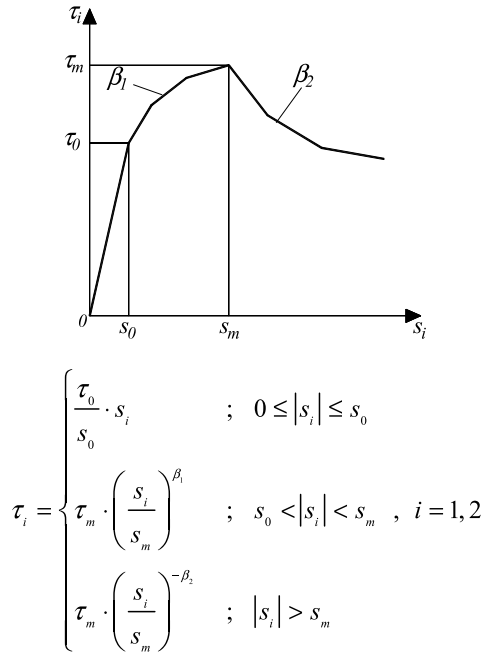
In addition to the force (F) applied at the shear span of 1.5 m, the self-weight was also considered based on the material's density ($\gamma_c = 2400 \times 9.81 = 23.5$ kN/m^3, $\gamma_s = 7850 \times 9.81 = 77.0$ kN/m^3).

The Newton-Raphson method with the arc-length technique was used to simulate the conditions of the real test, where the load was applied under displacement control. It was adopted an energy convergence tolerance of 1×10^{-3}. Fig. 25 shows the numerical curves of Force (F) versus deflection at loaded-section (δ) and concrete strain at the bottom reinforcement level of the loaded-section (ε) versus δ relationships obtained from the numerical simulations of T-cross section steel RSFRC beam. A maximum load of 328.84 kN was obtained from the numerical simulations. The midspan deflection was determined from the difference between the nodal displacement at geometric center of the loaded section and the average nodal displacement at the geometric center of the supported sections. The calculation of the strain at the bottom reinforcement level was determined with the interpolation of the nodal displacements at two sampling points.

In Fig. 26 is depicted the crack pattern obtained from the simulation, where is visible that the beam failed in shear, but the maximum strain at the level of the flexural reinforcement (2.14‰, Fig. 25) indicates that the yielding initiation of this reinforcement in

(a)

	Confined	Unconfined
τ_0 (MPa)	4.16	4.16
τ_m (MPa)	6.96	6.33
s_0 (mm)	0.2	0.2
s_m (mm)	0.725	0.571
β_1	0.4	0.4
β_2	0.3	10.0

$$\tau_i = \begin{cases} \dfrac{\tau_0}{s_0} \cdot s_i & ; \quad 0 \leq |s_i| \leq s_0 \\[2mm] \tau_m \cdot \left(\dfrac{s_i}{s_m}\right)^{\beta_1} & ; \quad s_0 < |s_i| < s_m \quad , \quad i = 1,2 \\[2mm] \tau_m \cdot \left(\dfrac{s_i}{s_m}\right)^{-\beta_2} & ; \quad |s_i| > s_m \end{cases}$$

(b)

Fig. 24. (a) Representation of the bars assigned with confined (red lines) and unconfined (blue lines) bond-slip properties; (b) Bond-slip relationship and parameters for the confined and unconfined regions of the bottom level steel reinforcements.
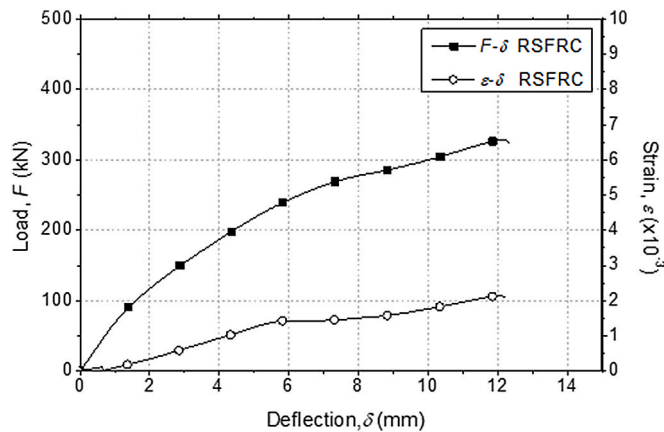

Fig. 25. F/ε - δ relationships obtained from numerical simulations of T-cross section steel RSFRC beam.

the loaded section (2.78‰, Fig. 23) was not too far. It is interesting to observe that the average of the maximum load carrying capacity of the two beams tested in the BSC was 334 kN, taking into account an ISFRC with 60 kg/m³ of hooked ends ISF.

According to the EC2 [52] recommendations, 42 conventional steel stirrups (21 on the beam flange and 21 on the beam web) were designed to assure the beam's shear capacity predicted in the numerical simulation, with 22 stirrups in the beam's critical span of 1.5 m (Ø6@140 mm) and 20 stirrups in the remaining 3.0 m of the beam span (Ø6@290 mm). The environmental impact of this shear reinforcement, which can be avoided using RSFRC, was estimated from an International EPD of carbon steel used as reinforce-
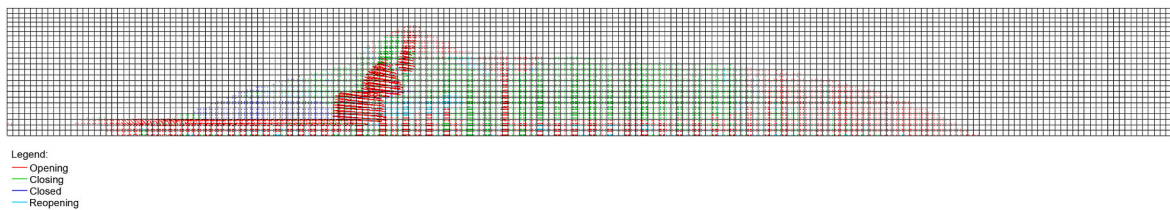
Fig. 26. Crack pattern at concrete failure of T-cross section steel RSFRC beam predicted by numerical simulation.

ment in concrete [56]. The analysis of the eight environmental impact categories presented in section 4.3 was performed at a product stage (raw material supply + transport + manufacturing) for the elimination of shear reinforcement (around 9.07 kg) and addition of RSF for RSFRC beam production (50.79 kg). The results obtained and the corresponding environmental benefit are presented in Tables 9 and 10. According to this, the environmental benefit of using RSFRC to reduce shear reinforcement is of 40% in GWP reduction. However, it is important to mention that these results are only at the product stage for one T-cross section beam. The difference would be more significant if an industrial scale of RSFRC beams production was considered. Additionally, the elimination of the shear reinforcement has also economic benefits related to the reduction of labor costs and construction time.

Conclusions

In the present study, the post-cracking constitutive laws of the RSFRC and ISFRC were derived by inverse analysis, by using the experimental curves obtained from 3PNBBT, RPT-3ps and DEWST performed in a previous study of the authors. The environmental impacts of RSFRC and ISFRC were evaluated using LCA methodology limited at raw material extraction and processing. From a material point of view, the RSFRC showed to be a technically viable solution, more environmentally sustainable than ISFRC of equal strength or composition.

The numerical simulations were able of fitting with high accuracy the experimental results to derive the tensile stress-crack width relationships of RSFRC and ISFRC that can be used on design approaches for RSFRC and ISFRC structures. According to the results obtained, RSFRC showed at least the same flexural and tensile performance as ISFRC.

Based on the LCA results, the reduction of the environmental impact of the production of 1 ton of RSF compared to ISF is clear for almost all environmental impact categories analyzed. For 1 m^3 of concrete, the RSFRC showed lower environmental impact than ISFRC with the same concrete matrix and equal volume of fibers, especially on the environmental impact categories of GWP, PE-Re, PE-NRe, POCP and ADP-Fossil fuels, with a corresponding lower impact of 17%, 20%, 28%, 34% and 34%, respectively. Comparing to commercial ISFRC, the RSFRC showed lower environmental impact than ISFRC with similar volume of fibers. Cement was the component that most negatively contributed to all environmental impact categories analyzed for RSFRC and ISFRC. However, the ISF production also had a significant contribution to the environmental impact, namely in the impact categories of GWP, POCP, AP, EP, ADP-Fossil fuels, PE-NRe and PE-Re. The ADP-Elements impact was significantly influenced by the amount of superplasticizer. Considering the performance functional unit of 1 MPa of indirect tensile strength, the RSFRC showed similar to lower environmental impact than ISFRC.

The bending performance of a T-cross section RSFRC beam with steel reinforcements was predicted by numerical simulation up to shear failure. A maximum flexural load of 328.84 kN was obtained and the results indicated that the yielding initiation of the flexural reinforcement was close to occurring in the loaded section. The use of RSFRC for industrial production of full-scale beams may have relevant technical, environmental and economic advantages in terms of shear reinforcement. In this case, an amount of 9.07 kg of

Table 9
Baseline CML method results for 9.07 kg of steel stirrups and 50.79 kg of RSF.

Material	GWP kg CO_2 - eq.	ODP kg CFC11 - eq.	POCPkg ethen - eq.	AP kg SO_2 - eq.	EPkg PO_4^{-3} − eq.	ADP	
						Elementskg Sb - eq.	Fossil fuels MJ
Steel stirrups	6.89	9.52×10^{-9}	1.85×10^{-3}	2.66×10^{-2}	2.73×10^{-3}	1.01×10^{-6}	80.07
RSF	2.78	4.38×10^{-7}	8.21×10^{-4}	1.66×10^{-2}	8.72×10^{-4}	6.91×10^{-8}	32.61
Environmental benefit	4.11	$- 4.29 \times 10^{-7}$	1.03×10^{-3}	9.96×10^{-3}	1.86×10^{-3}	9.37×10^{-7}	47.46

Table 10
Cumulative Energy Demand (CED) results for 1 MPa of indirect tensile strength.

Material	PE-NRe MJ	PE-Re MJ
Steel stirrups	80.07	12.69
RSF	50.32	0.78
Environmental benefit	29.75	11.92

steel stirrups was estimated to be avoided from each RSFRC beam with an associated environmental benefit of 40% in GWP reduction.

CRediT authorship contribution statement

Declaration of competing interest

The authors declare that they have no known competing financial interests or personal relationships that could have appeared to influence the work reported in this paper.

Acknowledgements

References

[1] P. de Wilde, D. Coley, The implications of a changing climate for buildings, Build. Environ. 55 (2012) 1–7, https://doi.org/10.1016/j.buildenv.2012.03.014.

[2] Global Alliance for Buildings and Construction (GlobalABC), International Energy Agency (Iea) and the United Nations (UN) Environment Programme, 2019 Global Status Report for Buiildings and Construction: Towards a zero-Emission, Efficient and Resilient Buildings and Construction Sector, IEA and UN Environment Programme, Switzerland, 2019, p. 39. https://www.worldgbc.org/news-media/2019-global-status-report-buildings-and-construction.

[3] J. Paris, J. Roessler, C. Ferraro, H. DeFord, T. Townsend, A review of waste products utilized as supplements to Portland cement in concrete, J. Clean. Prod. 121 (2016) 1–18, https://doi.org/10.1016/j.jclepro.2016.02.013.

[4] V. Letelier, E. Tarela, P. Muñoz, G. Moriconi, Combined effects of recycled hydrated cement and recycled aggregates on the mechanical properties of concrete, Construct. Build. Mater. 132 (2017) 365–375, https://doi.org/10.1016/j.conbuildmat.2016.12.010.

[5] O. Onuaguluchi, N. Banthia, Scrap tire steel fiber as a substitute for commercial steel fiber in cement mortar: engineering properties and cost-benefit analyses, Resour. Conserv. Recycl. 134 (2018) 248–256, https://doi.org/10.1016/j.resconrec.2018.03.014.

[6] J.A.O. Barros, C. Frazão, A. Caggiano, P. Folino, E. Martinelli, H. Xargay, Z. Zamanzadeh, L. Lourenço, Cementitious composites reinforced with recycled fibres, in: J.A.O. Barros, L. Ferrara (Eds.), Chapter 8 in Book "*Recent Advances On Green Concrete for Structural Purposes – the Contribution Of the EU-FP7 Project EnCoRe*", Springer Book, E. Martinelli, 2017, pp. 141–195, https://doi.org/10.1007/978-3-319-56797-6_8.

[7] K.M. Liew, A. Akbar, The recent progress of recycled steel fiber reinforced concrete, Construct. Build. Mater. 232 (2020) 117232, https://doi.org/10.1016/j.conbuildmat.2019.117232.

[8] A. Caggiano, P. Folino, C. Lima, E. Martinelli, M. Pepe, On the mechanical response of hybrid fiber reinforced concrete with recycled and industrial steel fibers, Construct. Build. Mater. 147 (2017) 286–295, https://doi.org/10.1016/j.conbuildmat.2017.04.160.

[9] H. Tlemat, K. Pilakoutas, K. Neocleous, Stress-strain characteristic of SFRC using recycled fibres, Mater. Struct. 39 (2006) 365–377, https://doi.org/10.1617/s11527-005-9009-4.

[10] A. Caggiano, H. Xargay, P. Folino, E. Martinelli, Experimental and numerical characterization of the bond behavior of steel fibers recovered from waste tires embedded in cementitious matrices, Cement Concr. Compos. 62 (2015) 146–155, https://doi.org/10.1016/j.cemconcomp.2015.04.015.

[11] M. Pajak, M. Krystek, M. Zakrzewski, J. Domski, Laboratory investigation and numerical modelling of concrete reinforced with recycled steel fibers, Materials 14 (2021) 1828, https://doi.org/10.3390/ma14081828.

[12] M. Pawelska-Mazur, M. Kaszynska, Mechanical performance and environmental assessment of sustainable concrete reinforced with recycled end-of-life tyre fibres, Materials 14 (2021) 256, https://doi.org/10.3390/ma14020256.

[13] S.G. Maxineasa, K. Neocleous, L. Dumitrescu, K. Themistocleous, N. Taranu, D. Hadjimitsis, Environmental LCA of innovative reuse of all end-of-life tyre components in concrete. Proceeding of the 1st International Conference on Construction Materials for Sustainable Future, Zadar, Croatia, 19-21 April 2017, 2017, pp. 941–947, 978-953-8168-04-8.

[14] World Business Council for Sustainable Development (WBCSD), End-of-Life Tires: A Framework for Effective Management Systems, Prepared by the WBCSD Tire Industry Project, Geneva, Switzerland, 2010. http://www.etrma.org/uploads/Modules/Documentsmanager/a-framework-for-effective-elt-management-systems-final-25.6.10.pdf.

[15] OECD, Transport Outlook 2012: Seamless Transport for Greener Growth. Prepared by the International Transport Forum (ITF), 2012, Paris, France. https://www.oecd.org/greengrowth/greening-transport/Transport%20Outlook%202012.pdf.

[16] M. Sienkiewicz, J. Kucinska-Lipka, H. Janik, A. Balas, Progress in used tyres management in the European Union: a review, Waste Manag. 32 (2012) 1742–1751, https://doi.org/10.1016/j.wasman.2012.05.010.

[17] V.L. Shulman (ETRA), Tire recycling, in: T.M. Letcher, D.A. Vallero (Eds.), Chapter 26 in Book "Waste: A Handbook For Management, second ed.", Academic Press, 2019, pp. 489–515, https://doi.org/10.1016/C2017-0-02201-2.

[18] A. Bentur, S. Mindess, Fibre Reinforced Cementitious Composites, second ed., Taylor & Francis, London, UK and New York, USA, 2007.

[19] V.M.C.F. Cunha, Steel Fibre Reinforced Self-Compacting Concrete (From Micro-mechanics to Composite Behaviour), Doctoral Thesis, Department of Civil Engineering, School of Engineering of the University of Minho, Guimarães, Portugal, 2010. http://hdl.handle.net/1822/10667.

[20] C. Frazão, A. Camões, J. Barros, D. Gonçalves, Durability of steel fiber reinforced self-compacting concrete, Construct. Build. Mater. 80 (2015) 155–166, https://doi.org/10.1016/j.conbuildmat.2015.01.061.

[21] H. Salehian, J.A.O. Barros, M. Taheri, Evaluation of the influence of post-cracking response of steel fibre reinforced concrete (SFRC) on load carrying capacity of SFRC panels, Construct. Build. Mater. 73 (2014) 289–304, https://doi.org/10.1016/j.conbuildmat.2014.09.043.

[22] C. Frazão, J. Barros, J.A. Bogas, K. Pilakoutas, C. de Sousa, An experimental investigation on the post-cracking behaviour of recycled steel fibre reinforced concrete. Fib bulletin 95-ACI-sp343: fibre reinforced concrete: from design to structural applications, in: Proceedings of the ACI-Fib-RILEM International

Workshop – FRC 2018, 2020, ISBN 978-2-88394-142-7, p. 539, https://doi.org/10.35789/fib.BULL.0095.

[23] L. Lourenço, Betão Reforçado com Fibras: aplicações e técnicas de inspeção e reforço de elementos estruturais afetados pela ação de um fogo, Doctoral thesis, Department of Civil Engineering, School of Engineering of the University of Minho, Guimarães, Portugal, 2012. http://hdl.handle.net/1822/2363.

[24] E. Pereira, Steel Fibre Reinforced Self-Compacting Concrete: from Material to Mechanical Behaviour, Dissertation for Pedagogical and Scientific Aptitude Proofs, Department Civil Engineering, University of Minho, 2006, p. 188.

[25] EN 14651, + A1 (2007). Test Method for Metallic Fibre Concrete - Measuring the Flexural Tensile Strength (Limit of Proportionality (LOP), Residual), CEN, Bruxelas, 2005.

[26] ASTM C1550-08, Standard Test Method for Flexural Toughness of Fiber Reinforced Concrete (Using Centrally Loaded Round Panel), ASTM International, USA, 2008.

[27] F. Minelli, G.A. Plizzari, in: B.H. Oh, et al. (Ed.), Fiber Reinforced Concrete Characterization through Round Panel Test – Part I: Experimental Study. Fracture Mechanics of Concrete and Concrete Structures – High Performance, Fiber Reinforced Concrete, Special Loadings and Structural Applications, 2010, Korea.

[28] M. di Prisco, L. Ferrara, M.L. Lamperti, Double edge wedge splitting (DEWS): an indirect tension test to identify post-cracking behaviour of fibre reinforced cementitious composites, Mater. Struct. 46 (11) (2013) 1893–1918, https://doi.org/10.1617/s11527-013-0028-2.

[29] A. Abrishambaf, J.A.O. Barros, V.M.C.F. Cunha, Tensile stress–crack width law for steel fibre reinforced self-compacting concrete obtained from indirect (splitting) tensile tests, Cement Concr. Compos. 57 (2015) 153–165, https://doi.org/10.1016/j.cemconcomp.2014.12.010.

[30] F. Micelli, M. Leone, G. Centonze, M. Aiello, Go green: using waste and recycling materials, in: Yang Lu (Ed.), Infrastructure Corrosion and Durability – A Sustainability Study, OMICS Group eBooks, USA, 2014, pp. 1–68.

[31] L.M.P. Matos, J.A.O. Barros, A. Ventura-Gouveia, R.A.B. Calçada, A new inverse analysis approach for predicting the fracture mode I parameters of fibre reinforced concrete, Eng. Fract. Mech. 246 (2021), 107613, https://doi.org/10.1016/j.engfracmech.2021.107613.

[32] Y. Wang, Mechanics of Fiber Reinforced Cementitious Composites, Doctoral Thesis, Department of Mechanical Engineering, Massachusetts Institute of Technology, 1989, p. 306. http://hdl.handle.net/1721.1/14296.

[33] A.F.M. Azevedo, J.A.O. Barros, J.M. Sena-Cruz, A.V. Gouveia, Software in structural engineering education and design, in: Proceedings of III Portuguese-Mozambican Conference of Engineering, 19-21 August, 2003, pp. 81–92, Mozambique.

[34] M. di Prisco, L. Ferrara, M.G.L. Lamperti, Double edge wedge splitting (DEWS): an indirect tension test to identify post-cracking behaviour of fiber reinforced cementitious composites, Mater. Struct. 46 (2013) 1893–1918, https://doi.org/10.1617/s11527-013-0028-2.

[35] ISO 14040, International Standard. Environmental Management - Life Cycle Assessment - Principles and Framework, ISO, Geneva, Switzerland, 2006.

[36] ISO 14044, International Standard. Environmental Management - Life Cycle Assessment - Requirements and Guidelines, ISO, Geneva, Switzerland, 2006.

[37] EN 15804, European standard, Sustainability of Construction Works - Environmental Product Declarations - Core Rules for the Product Category of Construction Products, CEN, Brussels, Belgium, 2012 + A1.

[38] J.D. Filippo, J. Karpman, J.R. DeShazo, The impacts of policies to reduce CO_2 emissions within the concrete supply chain, Cement Concr. Compos. 101 (2019) 67–82, https://doi.org/10.1016/j.cemconcomp.2018.08.003.

[39] S. Pushkar, Y. Ribakov, Life-cycle assessment of strengthening Pre-stressed normal-strength concrete beams with different steel-fibered concrete layers, Sustainability 12 (19) (2020) 7958, 2020, https://doi.org/10.3390/su12197958.

[40] B.L. Damineli, F.M. Kemeid, P.S. Aguiar, V.M. John, Measuring the eco-efficiency of cement use, Cement Concr. Compos. 32 (2010) 555–562, https://doi.org/10.1016/j.cemconcomp.2010.07.009.

[41] I.V. Muralikrishna, V. Manickam, Life Cycle Assessment. Chapter 5 in Book "Environmental Management - Science and Engineering for Industry", Butterworth-Heinemann, 2017, pp. 57–75.

[42] European Reference Life Cycle Database of the Joint Research Center, Version 3.2: Portland Cement (CEM I); CEMBUREAU Production Mix, at Plant, CEMBUREAU technology mix, 2015, EN 197-1.

[43] BauMineral GmbH, Environmental Product Declaration for Fly Ash, EFA-Füller MR3. BauMineral GmbH, 2017. https://www.baumineral.de/downloads/file/492/EPD-Baumineral-018-EFA-F%C3%BCller-MR3_ENG.pdf.

[44] EFCA, Environmental Product Declaration (EPD) Report. Concrete Admixtures – Plasticisers and Superplasticisers, European Federation of Concrete Admixtures Associations Ltd. (EFCA), 2015.

[45] R. Kurda, J.D. Silvestre, J.de Brito, Life cycle assessment of concrete made with high volume of recycled concrete aggregates and fly ash, Resour. Conserv. Recycl. 139 (2018) 407–417, https://doi.org/10.1016/j.resconrec.2018.07.004.

[46] A.M. Braga, J.D. Silvestre, J.de Brito, Compared environmental and economic impact from cradle to gate of concrete with natural and recycled coarse aggregates, J. Clean. Prod. 162 (2017) 529–543, https://doi.org/10.1016/j.jclepro.2017.06.057.

[47] J.B. Guinée, Handbook on Life Cycle Assessment: Operational Guide to the ISO Standards, Kluwer Academic Publishers, 2002.

[48] EPA, Life Cycle Assessment: Principles and Practice. Report EPA/600/R-06/060, EPA, Washington D.C., USA, 2006.

[49] C.B. Farinha, J.D. Silvestre, J. de Brito, M. do R. Veiga, Life cycle assessment of mortars with incorporation of industrial wastes, Fibers 7 (59) (2019) 19, https://doi.org/10.3390/fib7070059.

[50] J.D. Silvestre, Life Cycle Assessment "From Cradle to Cradle" of Building Assemblies – Application to External Walls, Doctoral Thesis. Instituto Superior Técnico, Lisbon, Portugal, 2012.

[51] Barros, et al., Blind competition on the numerical simulation of steel-fiber-reinforced concrete beams failing in shear. Structural Concrete Journal of the, fib (2020) 1–29, https://doi.org/10.1002/suco.202000345.

[52] EN 1992-1-1, Eurocode 2: Design of Concrete Structures - Part 1-1: General Rules and Rules for Buildings, European Standard, CEN, 2004.

[53] J. Sena-Cruz, J.A. Barros, Á.F. Azevedo, A.V. Gouveia, Numerical simulation of the nonlinear behavior of RC beams strengthened with NSM CFRP strips, in: Proceedings of CMNE/CILAMCE 2007, 13-15 June 2007, Oporto, APMTAC, Portugal, 2007. http://hdl.handle.net/1822/9129.

[54] A. Ventura-Gouveia, Constitutive Models for the Material Nonlinear Analysis of Concrete Structures Including Time Dependent Effects, PhD Thesis, Department of Civil Engineering, University of Minho, 2011.

[55] MC2010, CEB Fib Model Code 2010 - Final Draft, 2011, Switzerland.

[56] BREG EN EPD No000125, Environmental Product Declaration of Carbon Steel Reinforced Bar (Secondary Production Route – Scrap) provided by UK CARES in Accordance with the Requirements of EN 15804:2012 + A1:2013 and BRE Global Scheme Document SD207, 2020.